Mon. Not. R. Astron. Soc. **352,** 939–960 (2004) doi:10.1111/j.1365-2966.2004.07984.x

The 2dF Galaxy Redshift Survey: Wiener reconstruction of the cosmic web

Pirin Erdoğdu,[1,2⋆] Ofer Lahav,[1,18] Saleem Zaroubi,[3] George Efstathiou,[1] Steve Moody, John A. Peacock,[12] Matthew Colless,[17] Ivan K. Baldry,[9] Carlton M. Baugh,[16] Joss Bland-Hawthorn,[7] Terry Bridges,[7] Russell Cannon,[7] Shaun Cole,[16] Chris Collins,[4] Warrick Couch,[5] Gavin Dalton,[6,15] Roberto De Propris,[17] Simon P. Driver,[17] Richard S. Ellis,[8] Carlos S. Frenk,[16] Karl Glazebrook,[9] Carole Jackson,[17] Ian Lewis,[6] Stuart Lumsden,[10] Steve Maddox,[11] Darren Madgwick,[13] Peder Norberg,[14] Bruce A. Peterson,[17] Will Sutherland[12] and Keith Taylor[8] (the 2dFGRS Team)

[1]*Institute of Astronomy, Madingley Road, Cambridge CB3 0HA*
[2]*Department of Physics, Middle East Technical University, 06531, Ankara, Turkey*
[3]*Kapteyn Institute, University of Groningen, PO Box 800, 9700 AV, Groningen, the Netherlands*
[4]*Astrophysics Research Institute, Liverpool John Moores University, Twelve Quays House, Birkenhead L14 1LD*
[5]*Department of Astrophysics, University of New South Wales, Sydney, NSW 2052, Australia*
[6]*Department of Physics, University of Oxford, Keble Road, Oxford OX1 3RH*
[7]*Anglo-Australian Observatory, PO Box 296, Epping, NSW 2111, Australia*
[8]*Department of Astronomy, California Institute of Technology, Pasadena, CA 91025, USA*
[9]*Department of Physics and Astronomy, Johns Hopkins University, Baltimore, MD 21118-2686, USA*
[10]*Department of Physics, University of Leeds, Woodhouse Lane, Leeds LS2 9JT*
[11]*School of Physics and Astronomy, University of Nottingham, Nottingham NG7 2RD*
[12]*Institute for Astronomy, University of Edinburgh, Royal Observatory, Blackford Hill, Edinburgh EH9 3HJ*
[13]*Lawrence Berkeley National Laboratory, 1 Cyclotron Road, Berkeley, CA 94720, USA*
[14]*ETHZ Institut für Astronomie, HPF G3.1, ETH Hönggerberg, CH-8093 Zurich, Switzerland*
[15]*Rutherford Appleton Laboratory, Chilton, Didcot OX11 0QX*
[16]*Department of Physics, University of Durham, South Road, Durham DH1 3LE*
[17]*Research School of Astronomy and Astrophysics, The Australian National University, Weston Creek, ACT 2611, Australia*
[18]*Department of Physics and Astronomy, University College London, Gower Street, London WC1E 6BT*

Accepted 2004 May 3. Received 2004 April 30; in original form 2003 November 7

ABSTRACT

We reconstruct the underlying density field of the Two-degree Field Galaxy Redshift Survey (2dFGRS) for the redshift range $0.035 < z < 0.200$ using the Wiener filtering method. The Wiener filter suppresses shot noise and accounts for selection and incompleteness effects. The method relies on prior knowledge of the 2dF power spectrum of fluctuations and the combination of matter density and bias parameters, however the results are only slightly affected by changes to these parameters. We present maps of the density field. We use a variable smoothing technique with two different effective resolutions: 5 and 10 h^{-1} Mpc at the median redshift of the survey. We identify all major superclusters and voids in the survey. In particular, we find two large superclusters and two large local voids. The full set of colour maps can be viewed on the World Wide Web at http://www.ast.cam.ac.uk/∼pirin.

Key words: methods: statistical – galaxies: distances and redshifts – large-scale structure of Universe.

⋆E-mail: pirin@ast.cam.ac.uk

1 INTRODUCTION

Historically, redshift surveys have provided the data and the test ground for much of the research on the nature of clustering and the distribution of galaxies. In the past few years, observations of large-scale structure have improved greatly. Today, with the development of fibre-fed spectrographs that can simultaneously measure spectra of hundreds of galaxies, cosmologists have at their fingertips large redshift surveys such as Two-degree Field (2dF) and Sloan Digital Sky Survey (SDSS). The analysis of these redshift surveys yields invaluable cosmological information. On the quantitative side, with the assumption that the galaxy distribution arises from the gravitational instability of small fluctuations generated in the early Universe, a wide range of statistical measurements can be obtained, such as the power spectrum and bispectrum. Furthermore, a qualitative understanding of galaxy distribution provides insight into the mechanisms of structure formation that generate the complex pattern of sheets and filaments comprising the 'cosmic web' (Bond, Kofman & Pogosyan 1996) we observe, and allows us to map a wide variety of structure, including clusters, superclusters and voids.

Today, many more redshifts are available for galaxies than direct distance measurements. This discrepancy inspired a great deal of work on methods for reconstruction of the real-space density field from that observed in redshift space. These methods use a variety of functional representations (e.g. Cartesian, Fourier, spherical harmonics or wavelets) and smoothing techniques (e.g. a Gaussian or a top-hat sphere). There are physical as well as practical reasons why one would be interested in smoothing the observed density field. It is often assumed that the galaxy distribution samples the underlying smooth density field and the two are related by a proportionality constant, the so-called linear bias parameter, b. The finite sampling of the smooth underlying field introduces Poisson 'shot noise'.[1] Any robust reconstruction technique must reliably mitigate the statistical uncertainties due to shot noise. Moreover, in redshift surveys, the actual number of galaxies in a given volume is larger than the number observed, in particular in magnitude-limited samples where at large distances only very luminous galaxies can be seen.

In this paper, we analyse large-scale structure in the Two-degree Field Galaxy Redshift Survey (2dFGRS; Colless et al. 2001), which has now obtained the redshifts for approximately 230 000 galaxies. We recover the underlying density field, characterized by an assumed power spectrum of fluctuations, from the observed field which suffers from incomplete sky coverage (described by the angular mask) and incomplete galaxy sampling due to its magnitude limit (described by the selection function). The filtering is achieved by a Wiener filter (Wiener 1949; Press et al. 1992) within the framework of both linear and non-linear theory of density fluctuations. The Wiener filter is optimal in the sense that the variance between the derived reconstruction and the underlying true density field is minimized. As opposed to ad hoc smoothing schemes, the smoothing due to the Wiener filter is determined by the data. In the limit of high signal-to-noise, the Wiener filter modifies the observed data only weakly, whereas it suppresses the contribution of the data contaminated by shot noise.

Wiener filtering is a well-known technique and has been applied to many fields in astronomy (see Rybicki & Press 1992). For example, the method was used to reconstruct the angular distribution (Lahav et al. 1994), the real-space density, velocity and gravitational potential fields of the 1.2-Jy *IRAS* (Fisher et al. 1995) and *IRAS* PSCz surveys (Schmoldt et al. 1999). The Wiener filter was also applied to the reconstruction of the angular maps of the cosmic microwave background temperature fluctuations (Bunn et al. 1994; Tegmark & Efstathiou 1996; Bouchet & Gispert 1999). A detailed formalism of the Wiener filtering method as it pertains to the large-scale structure reconstruction can be found in Zaroubi et al. (1995).

This paper is structured as follows. We begin with a brief review of the formalism of the Wiener filter method. A summary of the 2dFGRS data set, the survey mask and the selection function are given in Section 3. In Section 4, we outline the scheme used to pixelize the survey. In Section 5, we give the formalism for the covariance matrix used in the analysis. After that, we describe the application of the Wiener filter method to the 2dFGRS and present detailed maps of the reconstructed field. In Section 7, we identify the superclusters and voids in the survey.

Throughout this paper, we assume a Λ cold dark matter (CDM) cosmology with $\Omega_{\rm m} = 0.3$ and $\Omega_\Lambda = 0.7$ and $H_0 = 100\ h^{-1}$ km s^{-1} Mpc^{-1}.

2 WIENER FILTER

In this section, we give a brief description of the Wiener filter method. For more details, we refer the reader to Zaroubi et al. (1995). Let us assume that we have a set of measurements, $\{d_\alpha\}(\alpha = 1, 2, \ldots N)$ which are a linear convolution of the true underlying signal, s_α, plus a contribution from statistical noise, ϵ_α, such that

$$d_\alpha = s_\alpha + \epsilon_\alpha. \tag{1}$$

The Wiener filter is defined as the linear combination of the observed data, which is closest to the true signal in a minimum variance sense. More explicitly, the Wiener filter estimate, $s_\alpha^{\rm WF}$, is given by $s_\alpha^{\rm WF} = F_{\alpha\beta}\, d_\beta$ where the filter is chosen to minimize the variance of the residual field, r_α:

$$\left\langle \left| r_\alpha^2 \right| \right\rangle = \left\langle \left| s_\alpha^{\rm WF} - s_\alpha \right|^2 \right\rangle. \tag{2}$$

It is straightforward to show that the Wiener filter is

$$F_{\alpha\beta} = \left\langle s_\alpha d_\gamma^\dagger \right\rangle \left\langle d_\gamma d_\beta^\dagger \right\rangle^{-1}, \tag{3}$$

where the first term on the right-hand side is the signal–data correlation matrix

$$\left\langle s_\alpha d_\gamma^\dagger \right\rangle = \left\langle s_\alpha s_\gamma^\dagger \right\rangle, \tag{4}$$

and the second term is the data–data correlation matrix

$$\left\langle d_\alpha d_\beta^\dagger \right\rangle = \left\langle s_\gamma s_\delta^\dagger \right\rangle + \left\langle \epsilon_\alpha \epsilon_\beta^\dagger \right\rangle. \tag{5}$$

In the above equations, we have assumed that the signal and noise are uncorrelated. From equations (3) and (5), it is clear that, in order to implement the Wiener filter, one must construct a prior which depends on the mean of the signal (which is zero by construction) and the variance of the signal and noise. The assumption of a prior may be alarming at first glance. However, slightly inaccurate values of Wiener filter will only introduce second-order errors to the full reconstruction (see Rybicki & Press 1992). The dependence of the Wiener filter on the prior can be made clear by defining signal and noise matrices as $C_{\alpha\beta} = \langle s_\alpha s_\beta^\dagger \rangle$ and $N_{\alpha\beta} = \langle \epsilon_\alpha \epsilon_\beta^\dagger \rangle$. With this

[1] Another popular model for galaxy clustering is the halo model where the linear bias parameter depends on the mass of the dark matter haloes where the galaxies reside. For this model, the mean number of galaxy pairs in a given halo is usually lower than the Poisson expectation.

notation, we can rewrite the equations above so that $\boldsymbol{s}^{\rm WF}$ is given as

$$\boldsymbol{s}^{\rm WF} = \mathbf{C}\,[\mathbf{C}+\mathbf{N}]^{-1}\,\mathbf{d}. \quad (6)$$

The mean square residual given in equation (2) can then be calculated as

$$\langle \boldsymbol{r}\boldsymbol{r}^{\dagger}\rangle = \mathbf{C}\,[\mathbf{C}+\mathbf{N}]^{-1}\,\mathbf{N}. \quad (7)$$

Formulated in this way, we see that the purpose of the Wiener filter is to attenuate the contribution of low signal-to-noise ratio data. The derivation of the Wiener filter given above follows from the sole requirement of minimum variance and requires only a model for the variance of the signal and noise. The Wiener filter can also be derived using the laws of conditional probability if the underlying distribution functions for the signal and noise are assumed to be Gaussian. For the Gaussian prior, the Wiener filter estimate is both the maximum posterior estimate and the mean field (see Zaroubi et al. 1995).

As several authors point out (e.g. Rybicki & Press 1992; Zaroubi 2002), the Wiener filter is a biased estimator because it predicts a null field in the absence of good data, unless the field itself has zero mean. Because we have constructed the density field to have zero mean, we are not worried about this bias. However, the observed field deviates from zero due to selection effects and so it is necessary to be aware of this bias in the reconstructions.

It is well known that the peculiar velocities of galaxies distort clustering pattern in redshift space. On small scales, the random peculiar velocity of each galaxy causes smearing along the line of sight, known as the Finger of God. On larger scales, there is compression of structures along the line of sight due to coherent infall velocities of large-scale structure induced by gravity. One of the major difficulties in analysing redshift surveys is the transformation of the position of galaxies from redshift space to real space. For all sky surveys, this issue can be addressed using several methods, for example the iterative method of Yahil, Strauss & Huchra (1991) and the modified Poisson equation of Nusser & Davis (1994). However, these methods are not applicable to surveys which are not all-sky as they assume that, in linear theory, the peculiar velocity of any galaxy is a result of the matter distribution around it, and the gravitational field is dominated by the matter distribution inside the volume of the survey. For a survey such as the 2dFGRS, within the limitation of linear theory where the redshift-space density is a linear transformation of the real-space density, a Wiener filter can be used to transform from redshift space to real space (see Fisher et al. 1995 and Zaroubi et al. 1995 for further details). This can be written as

$$s^{\rm WF}(r_\alpha) = \langle s(r_\alpha)d(s_\gamma)\rangle\langle d(s_\gamma)d(s_\beta)\rangle^{-1}d(s_\beta), \quad (8)$$

where the first term on the right-hand side is the cross-correlation matrix of real- and redshift-space densities and $\boldsymbol{s}(\boldsymbol{r})$ is the position vector in redshift space. It is worth emphasizing that this method is limited. Although the Wiener filter has the ability to extrapolate the peculiar velocity field beyond the boundaries of the survey, it still only recovers the field generated by the mass sources represented by the galaxies within the survey volume. It does not account for possible external forces outside the range of the extrapolated field. This limitation can only be overcome by comparing the 2dF survey with all sky surveys.

3 DATA

3.1 2dFGRS data

The 2dFGRS, now completed, is selected in the photometric $b_{\rm J}$ band from the Automated Plate Measuring (APM) galaxy survey (Maddox, Efstathiou & Sutherland 1990) and its subsequent extensions. The survey covers about 2000 deg^2 and is made up of two declination strips, one in the South Galactic Pole region (SGP) covering approximately $-37.^\circ5 < \delta < -22.^\circ5$, $325.^\circ0 < \alpha < 55.^\circ0$ and the other in the direction of the North Galactic Pole (NGP), spanning $-7.^\circ5 < \delta < 2.^\circ5$, $147.^\circ5 < \alpha < 222.^\circ5$. In addition to these contiguous regions, there are a number of randomly located circular two-degree fields scattered over the full extent of the low-extinction regions of the southern APM galaxy survey.

The magnitude limit at the start of the survey was set at $b_{\rm J} = 19.45$ but both the photometry of the input catalogue and the dust extinction map have been revised since. So, there are small variations in magnitude limit as a function of position over the sky, which are taken into account using the magnitude limit mask. The effective median magnitude limit, over the area of the survey, is $b_{\rm J} \approx 19.3$ (Colless et al. 2001).

We use the data obtained prior to 2002 May, when the survey was nearly complete. This includes 221 283 unique, reliable galaxy redshifts. We analyse a magnitude-limited sample with redshift limits $z_{\rm min} = 0.035$ and $z_{\rm max} = 0.20$. The median redshift is $z_{\rm med} \approx 0.11$. We use 167 305 galaxies in total, 98 129 in the SGP and 69 176 in the NGP. We do not include the random fields in our analysis.

The 2dFGRS data base and full documentation are available on the WWW at http://www.mso.anu.edu.au/2dFGRS/.

3.2 Mask and radial selection function of the 2dFGRS

The completeness of the survey varies according to the position in the sky due to unobserved fields, particularly at the survey edges, and unfibred objects in the observed fields because of collision constraints or broken fibres.

For our analysis, we make use of two different masks (Colless et al. 2001; Norberg et al. 2002). The first of these masks is the redshift completeness mask defined as the ratio of the number of galaxies for which redshifts have been measured to the total number of objects in the parent catalogue. This spatial incompleteness is illustrated in Fig. 1. The second mask is the magnitude limit mask which gives the extinction corrected magnitude limit of the survey at each position.

The radial selection function gives the probability of observing a galaxy for a given redshift and can be readily calculated from the galaxy luminosity function:

$$\Phi(L)\,{\rm d}L = \Phi^*\left(\frac{L}{L^*}\right)^{\alpha}\exp\left(-\frac{L}{L^*}\right)\frac{{\rm d}L}{L^*}. \quad (9)$$

Here, for the concordance model, $\alpha = -1.21 \pm 0.03$, $\log_{10} L_* = -0.4\,(-19.66 \pm 0.07 + 5\log_{10}(h))$ and $\Phi_* = 0.0161 \pm 0.0008\,h^3$ (Norberg et al. 2002).

The selection function can then be expressed as

$$\phi(r) = \frac{\int_{L(r)}^{\infty}\Phi(L)\,{\rm d}L}{\int_{L_{\rm min}}^{\infty}\Phi(L)\,{\rm d}L}, \quad (10)$$

where $L(r)$ is the minimum luminosity detectable at luminosity distance r (assuming the concordance model), evaluated for the concordance model, $L_{\rm min} = {\rm Min}[L(r), L_{\rm com}]$ and $L_{\rm com}$ is the minimum luminosity for which the catalogue is complete and varies as a function of position over the sky. For distances considered in this paper, where the deviations from the Hubble flow are relatively small, the selection function can be approximated as $\phi(r) \approx \phi(z_{\rm gal})$. Each

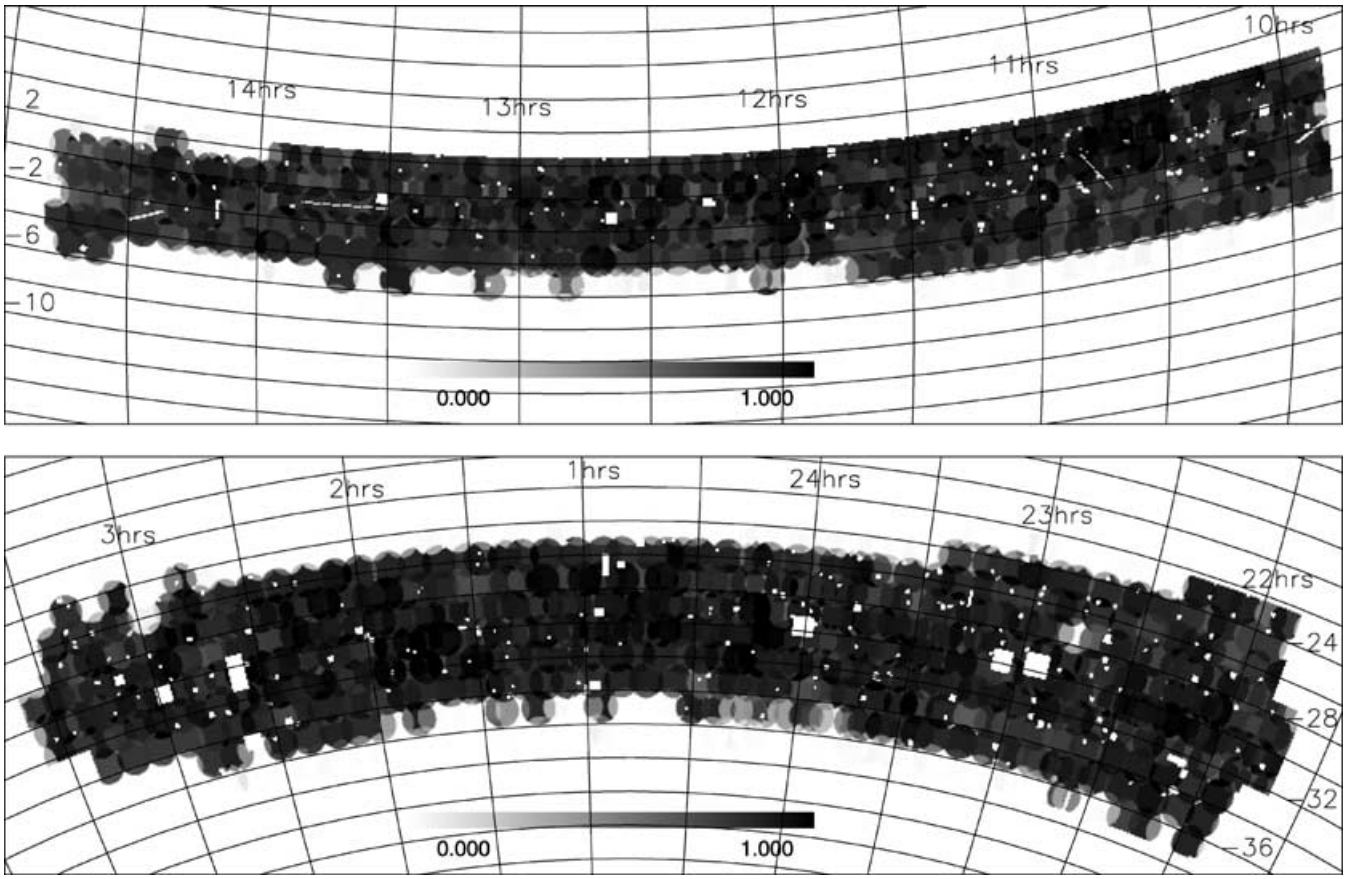

Figure 1. The redshift completeness masks for the NGP (top) and SGP (bottom) in equatorial coordinates. The grey-scale shows the completeness fraction.

galaxy, gal, is then assigned the weight

$$w(\mathrm{gal}) = \frac{1}{\phi(z_{\mathrm{gal}})M(\Omega_i)} \tag{11}$$

where $\phi(z_{\mathrm{gal}})$ and $M(\Omega_i)$ are the values of the selection function for each galaxy and angular survey mask for each cell i (see Section 4), respectively.

4 SURVEY PIXELIZATION

In order to form a data vector of overdensities, the survey needs to be pixelized. There are many ways to pixelize a survey: equal sized cubes in redshift space, igloo cells, spherical harmonics, Delauney tessellation methods, wavelet decomposition, etc. Each of these methods has its own advantages and disadvantages, and they should be treated with care as they form functional bases in which all the statistical and physical properties of cosmic fields are retained.

The pixelization scheme used in this analysis is an 'igloo' grid with wedge-shaped pixels in Cartesian space. Each pixel is bounded in right ascension, declination and redshift. The pixelization is constructed to keep the average number density per pixel approximately constant. The advantage of using this pixelization is that the number of pixels is minimized because the pixel volume is increased with redshift to counteract the decrease in the selection function. This is achieved by selecting a 'target cell width' for cells at the mean redshift of the survey and deriving the rest of the bin widths so as to match the shape of the selection function. The target cell widths used in this analysis are 10 and 5 h^{-1} Mpc. Once the redshift binning has been calculated, each radial bin is split into declination bands and then each band in declination is further divided into cells in right ascension. The process is designed so as to make the cells roughly cubical. Finally, the cell boundaries are converted to Cartesian coordinates for the analysis. In Fig. 2, we show an illustration of the method by plotting the cells in right ascension and declination for a given redshift strip.

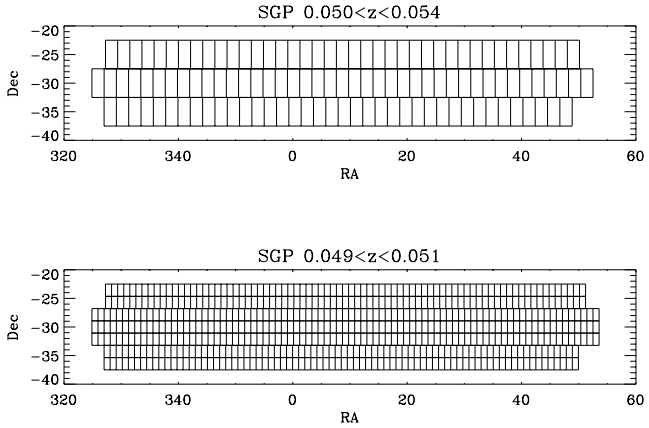

Figure 2. An illustration of the survey pixelization scheme used in the analysis, for 10 h^{-1} Mpc (top) and 5 h^{-1} Mpc (bottom) target cell widths. The redshift ranges are given on the top of each plot.

Although advantageous in many ways, the pixelization scheme used in this paper may complicate the interpretation of the reconstructed field. By definition, the Wiener filter signal will approach zero at the edges of the survey where the shot noise may dominate. This means the true signal will be constructed in a non-uniform manner. This effect will be amplified as the cell sizes become bigger at higher redshifts. Hence, both of these effects must be considered when interpreting the results.

5 ESTIMATING THE SIGNAL–SIGNAL CORRELATION MATRIX OVER PIXELS

The signal covariance matrix can be accurately modelled by an analytical approximation (Moody 2003). The calculation of the covariance matrix is similar to the analysis described by Efstathiou & Moody (2001) apart from the modification due to three-dimensionality of the survey. The covariance matrix for the 'noise-free' density fluctuations is $\langle C_{ij}\rangle = \langle \delta_i \delta_j \rangle$, where $\delta_i = (\rho_i - \bar{\rho})/\bar{\rho}$ in the ith pixel. It is estimated by first considering a pair of pixels with volumes V_i and V_j, separated by distance $\boldsymbol{r}$ so that

$$\langle C_{ij}\rangle = \left\langle \frac{1}{V_i V_j}\int_{\mathrm{Cell}_i}\delta(\boldsymbol{x})\,\mathrm{d}V_i \int_{\mathrm{Cell}_j}\delta(\boldsymbol{x}+\boldsymbol{r})\,\mathrm{d}V_j \right\rangle \tag{12}$$

$$= \frac{1}{V_i V_j}\int_{\mathrm{Cell}_i}\int_{\mathrm{Cell}_j}\langle\delta(\boldsymbol{x})\delta(\boldsymbol{x}+\boldsymbol{r})\rangle\,\mathrm{d}V_i\,\mathrm{d}V_j \tag{13}$$

$$= \frac{1}{V_i V_j}\int_{\mathrm{Cell}_i}\int_{\mathrm{Cell}_j}\xi(\boldsymbol{r})\;\mathrm{d}V_i\,\mathrm{d}V_j \tag{14}$$

where the isotropic two point correlation function $\xi(r)$ is given by

$$\xi(r) = \frac{1}{(2\pi)^3}\int P(k)\mathrm{e}^{-\mathrm{i}\boldsymbol{k}\cdot\boldsymbol{r}}\,\mathrm{d}^3k, \tag{15}$$

and therefore,

$$\langle C_{ij}\rangle = \frac{1}{(2\pi)^3 V_i V_j}\int P(k)\,\mathrm{d}^3k \times \int_{\mathrm{Cell}_i}\int_{\mathrm{Cell}_j}\mathrm{e}^{-\mathrm{i}\boldsymbol{k}(\boldsymbol{r}_i-\boldsymbol{r}_j)}\,\mathrm{d}V_i\,\mathrm{d}V_j. \tag{16}$$

After performing the Fourier transform, this equation can be written as

$$\langle C_{ij}\rangle = \frac{1}{(2\pi)^3}\int P(k)S(\boldsymbol{k},\boldsymbol{L}_i)S(\boldsymbol{k},\boldsymbol{L}_j)C(\boldsymbol{k},\boldsymbol{r})\,\mathrm{d}^3k, \tag{17}$$

where the functions S and C are given by

$$S(\boldsymbol{k},\boldsymbol{L}) = \mathrm{sinc}(k_xL_x/2)\mathrm{sinc}(k_yL_y/2)\mathrm{sinc}(k_zL_z/2) \tag{18}$$

$$C(\boldsymbol{k},\boldsymbol{r}) = \cos(k_xr_x)\cos(k_yr_y)\cos(k_zr_z). \tag{19}$$

Here, the label $\boldsymbol{L}$ describes the dimensions of the cell (L_x, L_y, L_z), the components of $\boldsymbol{r}$ describe the separation between cell centres, $\boldsymbol{k} = (k_x, k_y, k_z)$ is the wave vector and $\mathrm{sinc}(x) = (\sin(x))/x$. The wave vector, $\boldsymbol{k}$, is written in spherical coordinates k, θ, ϕ to simplify the evaluation of C. We define

$$k_x = k\sin(\phi)\cos(\theta) \tag{20}$$

$$k_y = k\sin(\phi)\sin(\theta) \tag{21}$$

$$k_z = k\cos(\phi). \tag{22}$$

Equation (17) can now be integrated over θ and ϕ to form the kernel $G_{ij}(k)$ where

$$G_{ij}(k) = \frac{1}{\pi^3}\int_0^{\pi/2}\int_0^{\pi/2} S(\boldsymbol{k},\boldsymbol{L}_i)S(\boldsymbol{k},\boldsymbol{L}_j)C(\boldsymbol{k},\boldsymbol{r}) \times \sin(\phi)\,\mathrm{d}\theta\,\mathrm{d}\phi, \tag{23}$$

so that

$$\langle C_{ij}\rangle = \int P(k)G_{ij}(k)k^2\,\mathrm{d}k. \tag{24}$$

In practice, we evaluate

$$\langle C_{ij}\rangle = \sum_k P_k G_{ijk}, \tag{25}$$

where P_k is the binned bandpower spectrum and G_{ijk} is

$$G_{ijk} = \int_{k_{\min}}^{k_{\max}} G_{ij}(k)\,k^2\,\mathrm{d}k, \tag{26}$$

where the integral extends over the band corresponding to the band power P_k.

For cells that are separated by a distance much larger than the cell dimensions, the cell window functions can be ignored, simplifying the calculation so that

$$G_{ijk} = \frac{1}{(2\pi)^3}\int_{k_{\min}}^{k_{\max}}\mathrm{sinc}(kr)\,4\pi k^2\,\mathrm{d}k, \tag{27}$$

where r is the separation between cell centres.

6 APPLICATION

6.1 Reconstruction using linear theory

In order to calculate the data vector $\boldsymbol{d}$ in equation (6), we first estimate the number of galaxies N_i in each pixel i

$$N_i = \sum_{\mathrm{gal}}^{N_{\mathrm{gal}}(i)} w(\mathrm{gal}), \tag{28}$$

where the sum is over all the observed galaxies in the pixel and w(gal) is the weight assigned to each galaxy (equation 11). The boundaries of each pixel are defined by the scheme described in Section 4, using a target cell width of $10\,h^{-1}$ Mpc. There are 13 480 cells in total (4526 in the NGP and 8954 in the SGP). The mean number of galaxies in pixel i is

$$\bar{N}_i = \bar{n}V_i, \tag{29}$$

where V_i is the volume of the pixel and the mean galaxy density, $\bar{n}$, is estimated using the equation

$$\bar{n} = \frac{\sum_{\mathrm{gal}}^{N_{\mathrm{total}}} w(\mathrm{gal})}{\int_0^\infty \mathrm{d}r r^2\phi(r)w(r)}, \tag{30}$$

where the sum is now over all the galaxies in the survey. We note that the value for $\bar{n}$ obtained using the equation above is consistent with the maximum estimator method proposed by Davis & Huchra (1982). Using these definitions, we write the ith component of the data vector $\boldsymbol{d}$ as

$$d_i = \frac{N_i - \bar{N}_i}{\bar{N}_i}. \tag{31}$$

Note that the mean value of $\boldsymbol{d}$ is zero by construction.

Reconstruction of the underlying signal given in equation (6) also requires the signal–signal and the inverse of the data–data

correlation matrices. The data–data correlation matrix (equation 5) is the sum of noise–noise correlation matrix **N** and the signal–signal correlation matrix **C** formulated in the previous section. The only change made is to the calculation of **C** where the real-space correlation function $\xi(r)$ is now multiplied by the Kaiser factor in order to correct for the redshift distortions on large scales. So

$$\xi_{\rm s} = \frac{1}{(2\pi)^3}\int P^{\rm S}(k)\exp[{\rm i}\boldsymbol{k}\cdot(\boldsymbol{r_2}-\boldsymbol{r_1})]\,{\rm d}^3k, \tag{32}$$

where $P^{\rm S}(k)$ is the galaxy power spectrum in redshift space

$$P^{\rm S}(k) = K[\beta]P^{\rm R}(k), \tag{33}$$

derived in linear theory. The superscripts 'R' and 'S' in this equation (and hereafter) denote real and redshift space, respectively.

$$K[\beta] = 1+\frac{2}{3}\beta+\frac{1}{5}\beta^2 \tag{34}$$

is the direction averaged Kaiser (1987) factor, derived using a distant observer approximation and with the assumption that the data subtend a small solid angle with respect to the observer (the latter assumption is valid for the 2dFGRS but does not hold for a wide angle survey; see Zaroubi & Hoffman, 1996 for a full discussion). Equation (33) shows that, in order to apply the Wiener filter method, we need a model for the galaxy power spectrum in redshift space which depends on the real-space power spectrum and on the redshift distortion parameter, $\beta \equiv \Omega_{\rm m}^{0.6}/b$.

The real-space galaxy power spectrum is well described by a scale invariant CDM power spectrum with shape parameter, Γ, for the scales concerned in this analysis. For Γ, we use the value derived from the 2dF survey by Percival et al. (2001) who fitted the 2dFGRS power spectrum over the range of linear scales using the fitting formulae of Eisenstein & Hu (1998). Assuming a Gaussian prior on the Hubble constant $h = 0.7 \pm 0.07$ (based on Freedman et al. 2001), they find $\Gamma = 0.2 \pm 0.03$. The normalization of the power spectrum is conventionally expressed in terms of the variance of the density field in spheres of 8 h^{-1} Mpc, σ_8. Lahav et al. (2002) use 2dFGRS data to deduce $\sigma_{8{\rm g}}^{\rm S}(L_{\rm s}, z_{\rm s}) = 0.94 \pm 0.02$ for the galaxies in redshift space, assuming $h = 0.7 \pm 0.07$ at $z_{\rm s} \approx 0.17$ and $L_{\rm s} \approx 1.9L^*$. We convert this result to real space using the following equation

$$\sigma_{8{\rm g}}^{\rm R}(L_{\rm s}, z_{\rm s}) = \sigma_{8{\rm g}}^{\rm S}(L_{\rm s}, z_{\rm s})/K^{1/2}[\beta(L_{\rm s}, z_{\rm s})] \tag{35}$$

where $K[\beta]$ is the Kaiser factor. For our analysis, we need to use σ_8 evaluated at the mean redshift of the survey for galaxies with luminosity L^*. However, it is necessary to assume a model for the evolution of galaxy clustering in order to find σ_8 at different redshifts. Moreover, the conversion from $L_{\rm s}$ to L^* introduces uncertainties in the calculation. Therefore, we choose an approximate value, $\sigma_{8{\rm g}}^{\rm R} \approx 0.8$ to normalize the power spectrum. For β, we adopt the value found by Hawkins et al. (2003), $\beta(L_{\rm s}, z_{\rm s}) = 0.49 \pm 0.09$ which is estimated at the effective luminosity, $L_{\rm s} \approx 1.4L^*$, and the effective redshift, $z_{\rm s} \approx 0.15$, of the survey sample. Our results are not sensitive to minor changes in σ_8 and β.

The other component of the data–data correlation matrix is the noise correlation matrix **N**. Assuming that the noise in different cells is not correlated, the only non-zero terms in **N** are the diagonal terms given by the variance – the second central moment – of the density error in each cell:

$$\mathcal{N}_{ii} = \frac{1}{\bar{N}_i^2}\sum_{\rm gal}^{N_{\rm gal}(i)} w^2({\rm gal}). \tag{36}$$

The final aspect of the analysis is the reconstruction of the real-space density field from the redshift-space observations. This is achieved using equation (8). Following Kaiser (1987), using distant observer and small-angle approximation, the cross-correlation matrix in equation (8) for the linear regime can be written as

$$\langle s(\boldsymbol{r})d(\boldsymbol{s})\rangle = \langle \delta_r \delta_s\rangle = \xi(r)\left(1+\frac{1}{3}\beta\right), \tag{37}$$

where $\boldsymbol{s}$ and $\boldsymbol{r}$ are position vectors in redshift and real space, respectively. The term $(1 + (1/3)\beta)$ is easily obtained by integrating the direction-dependent density field in redshift space. Using equation (37), the transformation from redshift space to real space simplifies to

$$s^{\rm WF}(\boldsymbol{r}) = \frac{1+(1/3)\beta}{K[\beta]}\mathbf{C}\,[\mathbf{C}+\mathbf{N}]^{-1}\,\mathbf{d}. \tag{38}$$

As mentioned earlier, the equation above is calculated for linear scales only and hence small-scale distortions (i.e. Fingers of God) are not corrected for. For this reason, we collapse in redshift space the fingers seen in 2dF groups (Eke et al. 2003) with more than 75 members, 25 groups in total (11 in the NGP and 14 in the SGP). All the galaxies in these groups are assigned the same coordinates. As expected, correcting these small-scale distortions does not change the constructed fields substantially as these distortions are practically smoothed out because of the cell size used in binning the data.

The maps shown in this section were derived by the technique detailed above. There are 80 sets of plots which show the density fields as strips in RA and Dec., 40 maps for the SGP and 40 maps for the NGP. Here we just show some examples; the rest of the plots can be found at http://www.ast.cam.ac.uk/∼pirin. For comparison, the top plots of Figs 3, 4, 5 and 6 show the redshift-space density field weighted by the selection function and the angular mask. The contours are spaced at $\Delta\delta = 0.5$ with solid (dashed) lines denoting positive (negative) contours; the heavy solid contours correspond to $\delta = 0$. Also plotted for comparison are the galaxies (dots) and the groups with $N_{\rm gr}$ number of members (Eke et al. 2003) and $9 \leqslant N_{\rm gr} \leqslant 17$ (circles), $18 \leqslant N_{\rm gr} \leqslant 44$ (squares) and $45 \leqslant N_{\rm gr}$ (stars). We also show the number of Abell, APM and Edinburgh–Durham Cluster Catalogue (EDCC) clusters studied by De Propris et al. (2002) (upside-down triangles). The middle plots show the redshift-space density shown in top plots after the Wiener filter is applied. As expected, the Wiener filter suppresses the noise. The smoothing performed by the Wiener filter is variable and increases with distance. The bottom plots show the reconstructed real density field $\boldsymbol{s}^{\rm WF}(\boldsymbol{r})$, after correcting for the redshift distortions. Here the amplitude of density contrast is reduced slightly. We also plot the reconstructed fields in declination slices. These plots are shown in Figs 7 and 8.

We also plot the square root of the variance of the residual field (equation 2), which defines the scatter around the mean reconstructed field. We plot the residual fields corresponding to some of the redshift slices shown in this paper (Figs 9 and 10). For better comparison, plots are made so that the cell number increases with increasing RA. If the volume of the cells used to pixelize the survey was constant, we would expect the square root of the variance $\Delta\delta$ to increase due to the increase in shot noise (equation 7). However, because the pixelization was constructed to keep the shot noise per pixel approximately constant, $\Delta\delta$ also remains constant ($\Delta\delta \approx 0.23$ for both the NGP and SGP) but the average density contrast in each pixel decreases with increasing redshift. This means that, although the variance of the residual in each cell is roughly equal, the relative variance (represented by $\Delta\delta/\delta$) increases with increasing redshift. This increase is clearly evident in Figs 9 and 10. Another conclusion that can be drawn from the figures is that the bumps in the density field are due to real features not due to error in the reconstruction, even at higher redshifts.

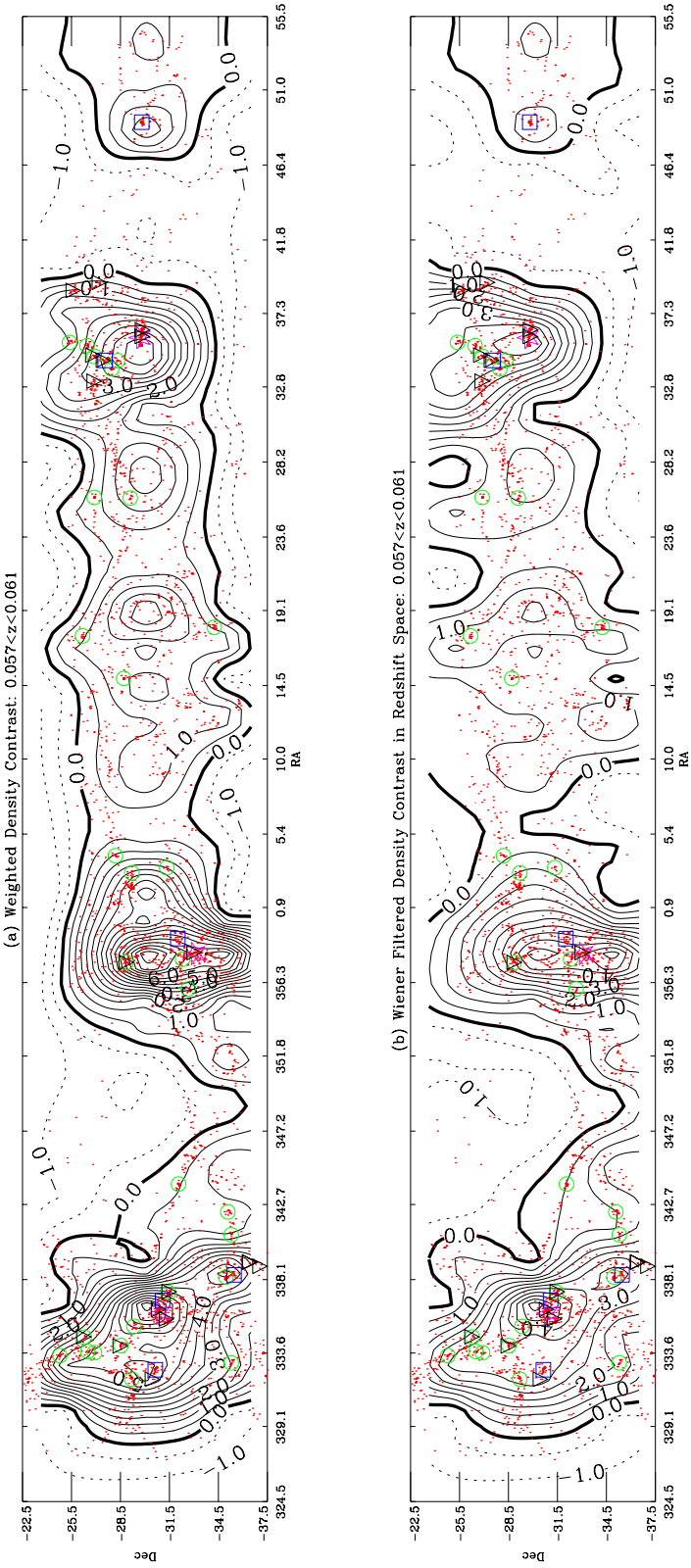

Figure 3. Reconstructions of the 2dFGRS SGP region for the redshift range $0.057 \leqslant z \leqslant 0.061$ for $10\,h^{-1}$ Mpc target cell size. The contours are spaced at $\Delta\delta = 0.5$ with solid (dashed) lines denoting positive (negative) contours; the heavy solid contours correspond to $\delta = 0$. The dots denote the galaxies with redshifts in the plotted range. (a) Redshift-space density field weighted by the selection function and the angular mask. (b) Same as in (a) but smoothed by a Wiener filter. (c) Same as in (b) but corrected for the redshift distortion. The overdensity centred (1) on RA $\approx$ 336$^{\rm h}$.5, Dec. $\approx -30^{\circ}.0$ is SCSGP03 (see Table 1), (2) on RA $\approx 0^{\rm h}.0$, Dec. $\approx -30^{\circ}.0$ is SCSGP04 (this overdensity is part of the Pisces–Cetus supercluster, and (3) on RA $\approx$ 36$^{\rm h}$.0, Dec. $\approx -29^{\circ}.3$ is SCSGP05. The underdensity centred on RA $\approx$ 350$^{\rm h}$.0, Dec. $\approx -30^{\circ}.0$ is VSGP12 (see Table 2).

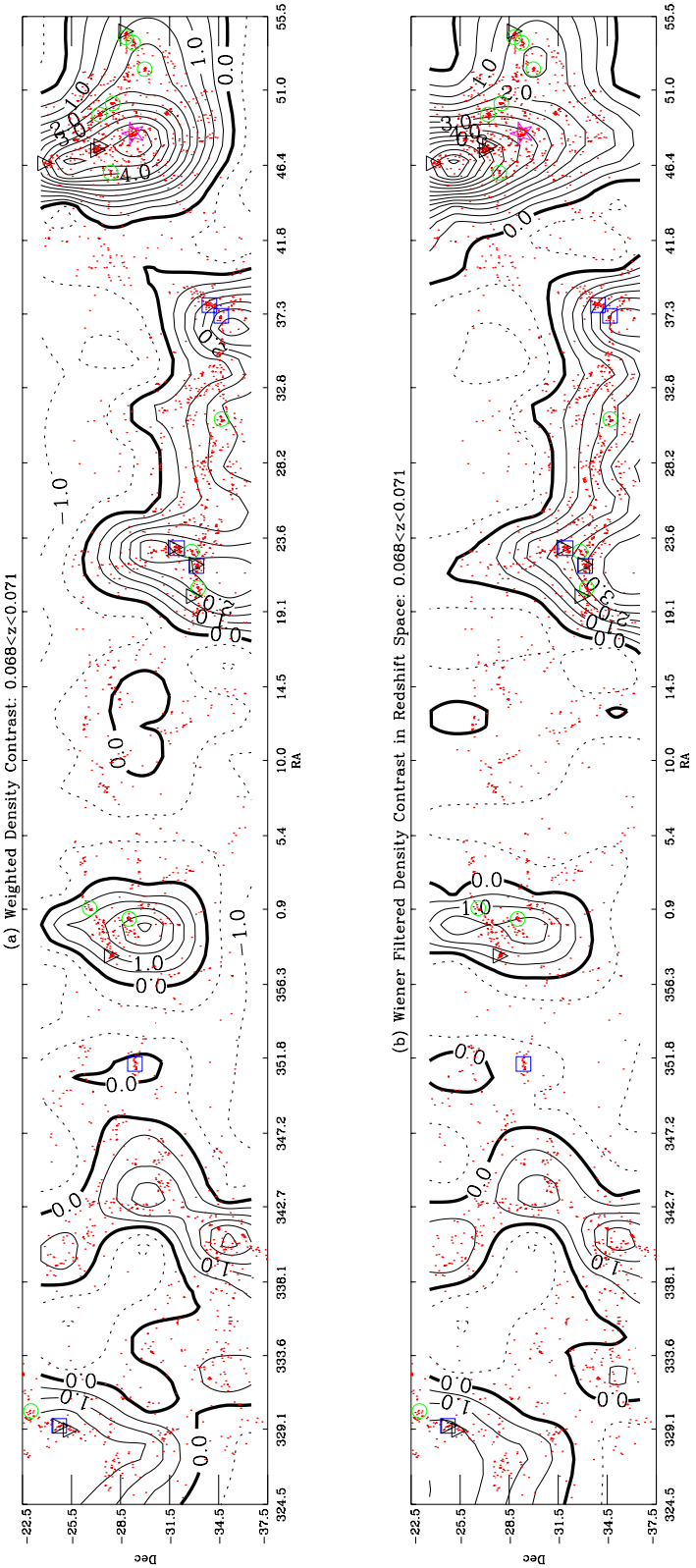

Figure 4. Reconstructions of the 2dFGRS SGP region for the redshift range $0.068 \leqslant z \leqslant 0.071$ for $10\,h^{-1}$ Mpc target cell size. Same as in Fig. 3. The overdensity centred (1) on RA $\approx 39\overset{\circ}{.}0$, Dec. $\approx -34\overset{\circ}{.}5$ is SCSGP07 (see Table 1) and is part of the Leo–Coma supercluster, and (2) on RA $\approx 0\overset{\circ}{.}0$, Dec. $\approx -30\overset{\circ}{.}0$ is SCSGP06 and is part of Horoglium Reticulum supercluster (see Table 1).

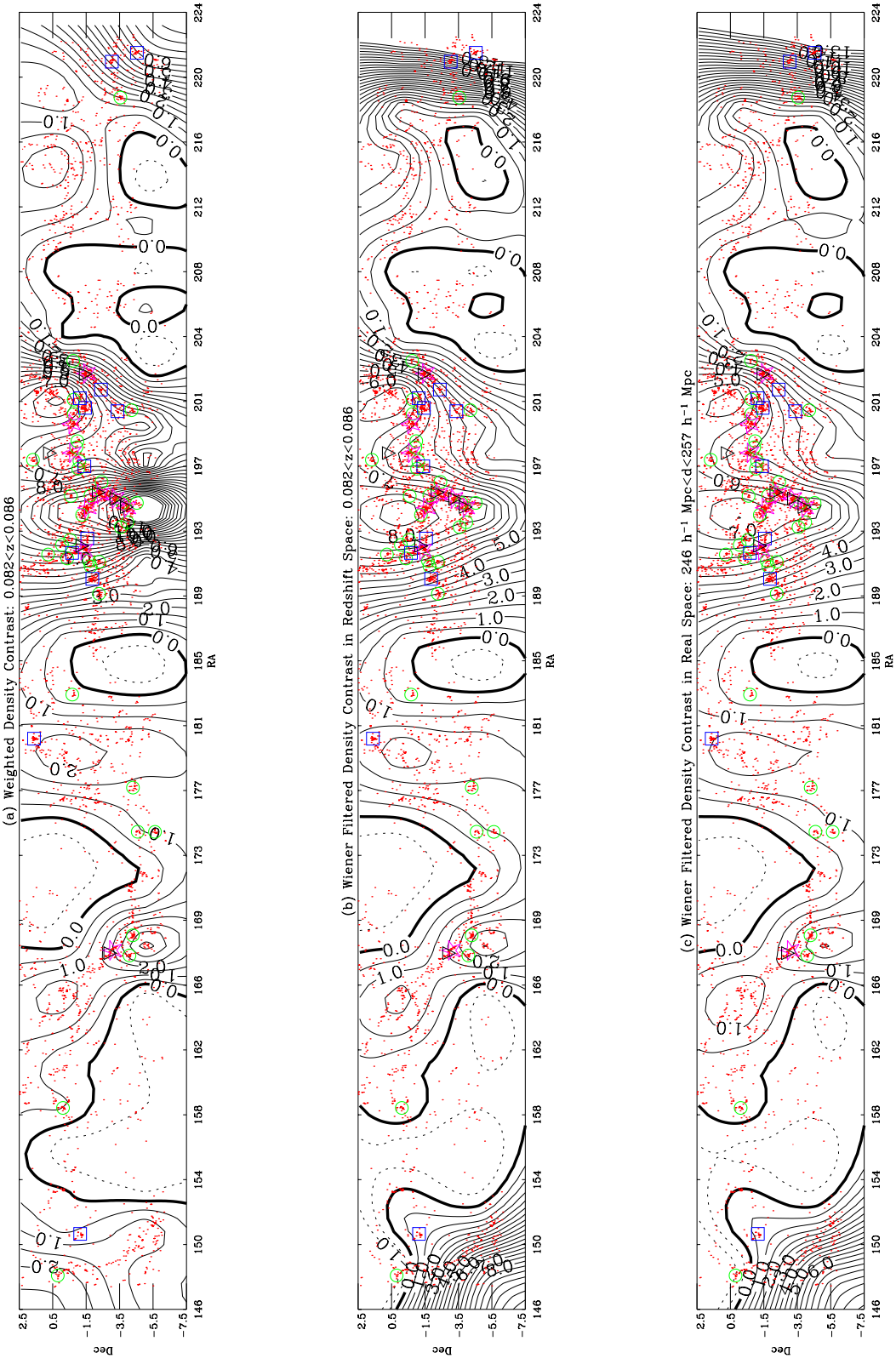

Figure 5. Reconstructions of the 2dFGRS NGP region for the redshift range $0.082 \leqslant z \leqslant 0.086$ for 10 h^{-1} Mpc target cell size. Same as in Fig. 3. The overdensity centred on RA $\approx 194^{\rm h}0$, Dec. $\approx -2^{\circ}5$ is SCNGP06 (see Table 1).

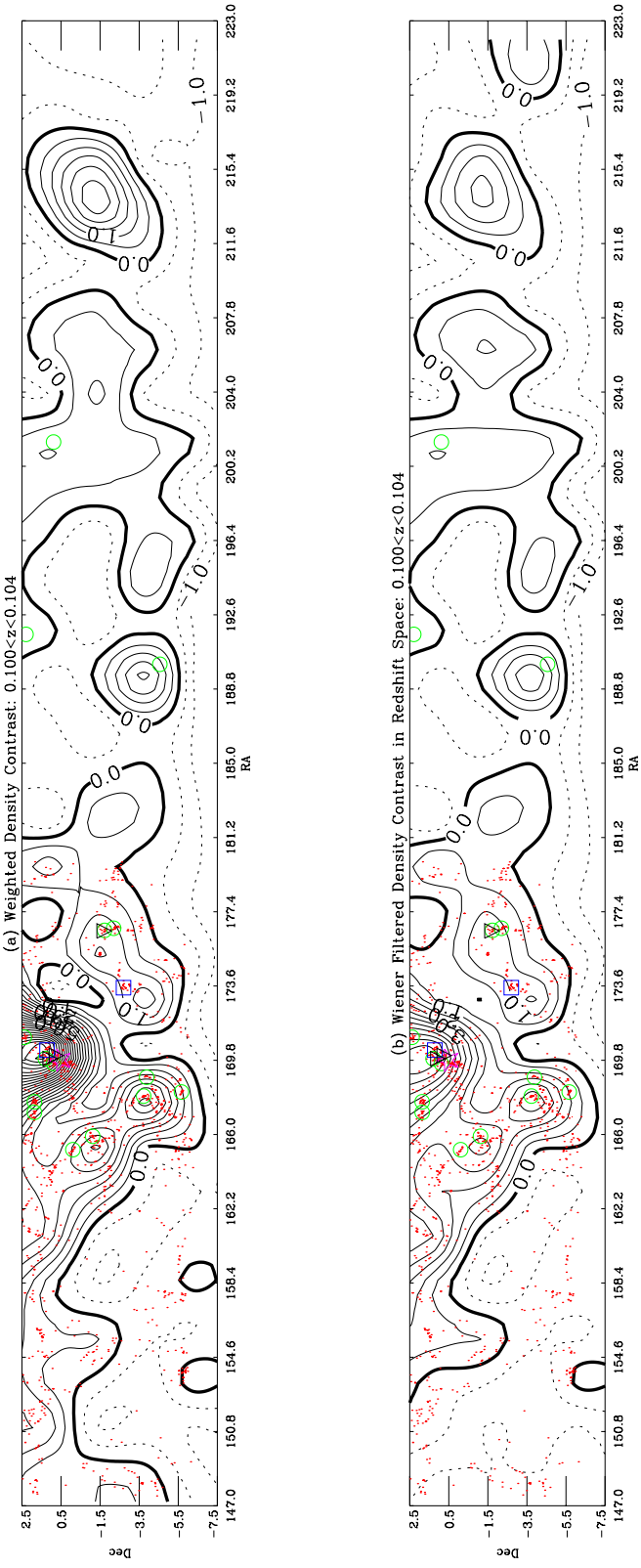

Figure 6. Reconstructions of the 2dFGRS NGP region for the redshift range $0.100 \leqslant z \leqslant 0.104$ for $10\,h^{-1}$ Mpc target cell size. Same as in Fig. 3. The overdensity centred (1) on RA $\approx 170^{\circ}.0$, Dec. $\approx -1^{\circ}.0$ is SCNGP08 (see Table 1). The underdensity centred (1) on RA $\approx 150^{\circ}.0$, Dec. $\approx -1^{\circ}.5$ is VNGP18 (see Table 3), (2) on RA $\approx 192^{\circ}.5$, Dec. $\approx 0^{\circ}.5$ is VNGP19, and (3) on RA $\approx 209^{\circ}.0$, Dec. $\approx -1^{\circ}.5$ is VNGP17.

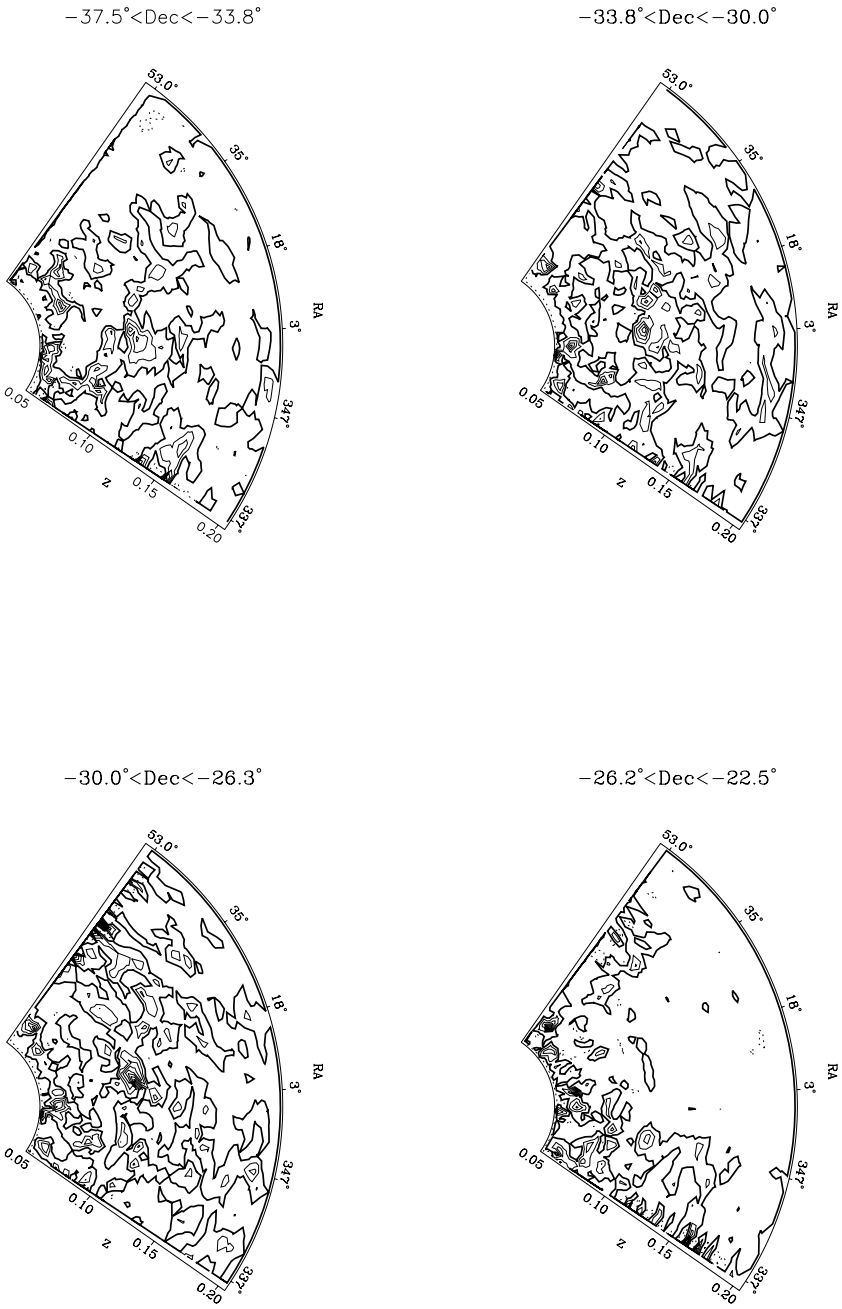

Figure 7. Reconstructions of the 2dFGRS SGP region in slices of declination for 10 h^{-1} Mpc target cell size. The declination range is given on the top of each plot. The contours are spaced at $\Delta\delta = 1.0$ with solid (dashed) lines denoting positive (negative) contours; the heavy solid contours correspond to $\delta = 0$.

We also use the χ^2 statistic in order to check the consistency of the model with the data. χ^2 is defined by

$$\chi^2 = \mathbf{d}^\dagger(\mathbf{S} + \mathbf{N})^{-1}\mathbf{d}. \tag{39}$$

A value χ^2 that is of the order of the number of degrees of freedom (dof) means that the model and the data are consistent. In this analysis, the number of dof equals the number of pixels. We find $\chi^2/\mathrm{dof} = 1.06$. This value indicates that the data and the model are in very good agreement.

6.2 Reconstruction using non-linear theory

In order to increase the resolution of the density field maps, we reduce the target cell width to 5 h^{-1} Mpc. A volume of a cubic cell of side 5 h^{-1} Mpc is roughly equal to a top-hat sphere of radius of about 3 h^{-1} Mpc. The variance of the mass density field in this sphere is $\sigma_3 \approx 1.7$ which corresponds to non-linear scales. To reconstruct the density field on these scales, we require accurate descriptions of the non-linear galaxy power spectrum and the non-linear redshift space distortions.

For the non-linear matter power spectrum $P^{\mathrm{R}}_{\mathrm{nl}}(k)$, we adopt the empirical fitting formula of Smith et al. (2003). This formula, derived using the 'halo model' for galaxy clustering, is more accurate than the widely used Peacock & Dodds (1996) fitting formula, which is based on the assumption of 'stable clustering' of virialized haloes. We note that for the scales concerned in this paper (up to $k \approx 10\ h$ Mpc^{-1}), Smith et al. (2003) and Peacock & Dodds (1996) fitting formulae give very similar results. For simplicity we assume linear,

Figure 8. Reconstructions of the 2dFGRS NGP region in slices of declination for 10 h^{-1} Mpc target cell size. The declination range is given on the top of each plot. The contours are spaced at $\Delta\delta = 1.0$ with solid (dashed) lines denoting positive (negative) contours; the heavy solid contours correspond to $\delta = 0$.

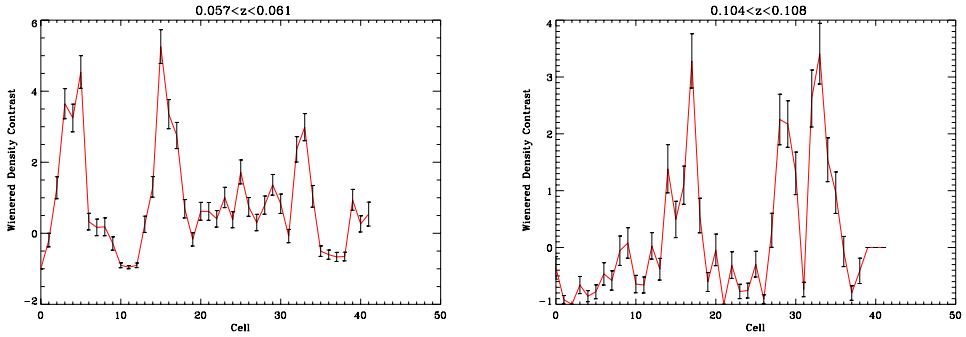

Figure 9. The plot of overdensities in the SGP for each redshift slice for the 10 h^{-1} Mpc target cell size shown. Also plotted are the variances of the residual associated for each cell. The increase in cell number indicates the increase of RA in each redshift slice.

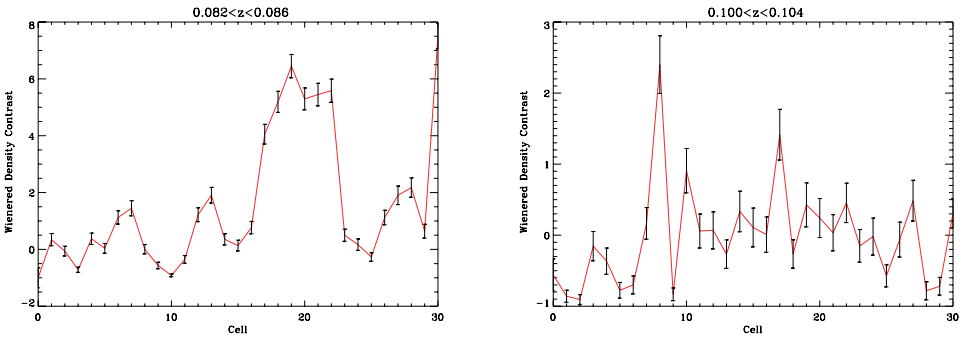

Figure 10. Same as in Fig. 9 but for the redshift slices in the NGP shown above.

scale-independent biasing in order to determine the galaxy power spectrum from the mass power spectrum, where b measures the ratio between galaxy and mass distribution:

$$P_{\rm nl}^{\rm R}(k) = b^2 P_{\rm nl}^{m}(k). \tag{40}$$

Here, $P_{\rm nl}^{\rm R}(k)$ is the galaxy and $P_{\rm nl}^{m}(k)$ is the matter power spectrum. We assume that $b = 1.0$ for our analysis. While this value is in agreement with the result obtained from the 2dFGRS (Lahav et al. 2002; Verde et al. 2002) for scales of tens of Mpc, it does not hold true for the scales of 5 h^{-1} Mpc on which different galaxy populations show different clustering patterns Madgwick et al. 2002; Norberg et al. 2002; Zehavi et al. 2002). More realistic models exist where biasing is scale-dependent (e.g. Peacock & Smith 2000; Seljak 2000) but because the Wiener filtering method is not sensitive to small errors in the prior parameters and the reconstruction scales are not highly non-linear, the simple assumption of no bias will still give accurate reconstructions.

The main effect of redshift distortions on non-linear scales is the reduction of power as a result of radial smearing due to virialized motions. The density profile in redshift space is then the convolution of its real-space counterpart with the peculiar velocity distribution along the line of sight, leading to damping of power on small scales. This effect is known to be reasonably well approximated by treating the pairwise peculiar velocity field as Gaussian or better still as an exponential in real space (superpositions of Gaussians), with dispersion $\sigma_{\rm p}$ (e.g. Peacock & Dodds 1994; Ballinger, Peacock & Heavens 1996; Kang et al. 2002). Therefore the galaxy power spectrum in redshift space is written as

$$P_{\rm nl}^{\rm S}(k,\mu) = P_{\rm nl}^{\rm R}(k,\mu)(1+\beta\mu^2)^2 D(k\sigma_{\rm p}\mu), \tag{41}$$

where μ is the cosine of the wave vector to the line of sight, $\sigma_{\rm p}$ has the unit of h^{-1} Mpc and the damping function in k-space is a Lorentzian:

$$D(k\sigma_{\rm p}\mu) = \frac{1}{1+\left(k^2\sigma_{\rm p}^2\mu^2\right)/2}. \tag{42}$$

Integrating equation (41) over μ, we obtain the direction-averaged power spectrum in redshift space:

$$\frac{P_{\rm nl}^{\rm S}(k)}{P_{\rm nl}^{\rm R}(k)} = \frac{4\left(\sigma_{\rm p}^2k^2-\beta\right)\beta}{\sigma_{\rm p}^4k^4} + \frac{2\beta^2}{3\sigma_{\rm p}^2k^2} + \frac{\sqrt{2}\left(k^2\sigma_{\rm p}^2-2\beta\right)^2\arctan(k\sigma_{\rm p}/\sqrt{2})}{k^5\sigma_{\rm p}^5}. \tag{43}$$

For the non-linear reconstruction, we use equation (43) instead of equation (33) when deriving the correlation function in redshift space. Fig. 11 shows how the non-linear power spectrum is damped in redshift space (dashed line) and compared to the linear power spectrum (dotted line). In this plot and throughout this paper we adopt the $\sigma_{\rm p}$ value derived by Hawkins et al. (2003), $\sigma_{\rm p} = 506 \pm 52$ km s^{-1}. Interestingly, by coincidence, the non-linear and linear power spectra look very similar in redshift space. So, if we had used the linear power spectrum instead of its non-linear counterpart, we still would have obtained physically accurate reconstructions of the density field in redshift space.

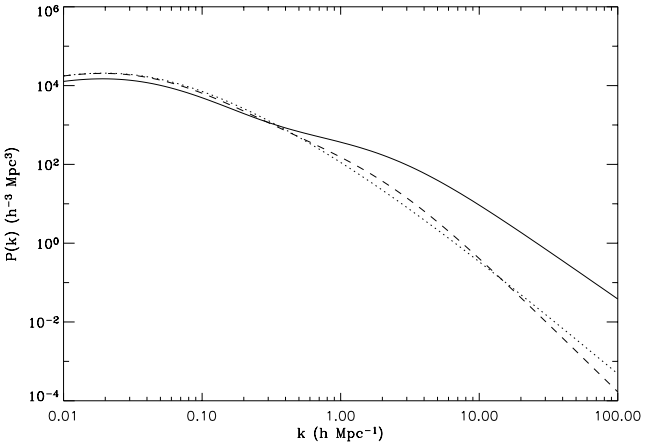

Figure 11. Non-linear power spectra for $z = 0$ and the concordance model with $\sigma_{\rm p} = 506$ km s^{-1} in real space (solid line), in redshift space from equation (43) (dashed line), both derived using the fitting formulae of Smith et al. (2003) and linear power spectra in redshift space derived using linear theory and the Kaiser factor (dotted line).

The optimal density field in real space is calculated using equation (8). The cross-correlation matrix in equation (38) can now be approximated as

$$\langle \boldsymbol{s}(\boldsymbol{r})\boldsymbol{d}(\boldsymbol{s})\rangle = \xi(r,\mu)(1+\beta\mu^2)\sqrt{D(k\sigma_{\rm p}\mu)}. \tag{44}$$

Again, integrating the equation above over μ, the direction averaged cross-correlation matrix of the density field in real space and the density field in redshift space can be written as

$$\frac{\langle \boldsymbol{s}(\boldsymbol{r})\boldsymbol{d}(\boldsymbol{s})\rangle}{\langle \boldsymbol{s}(\boldsymbol{r})\boldsymbol{s}(\boldsymbol{r})\rangle} = \frac{1}{2k^2\sigma_{\rm p}^2}\ln\left[k^2\sigma_{\rm p}^2\left(1+\sqrt{1+1/k^2\sigma_{\rm p}^2}\right)\right] + \frac{\beta}{k^2\sigma_{\rm p}^2}\sqrt{1+k^2\sigma_{\rm p}^2} + \frac{\beta}{k^3\sigma_{\rm p}^3}\,\mathrm{arcsinh}\left(k^2\sigma_{\rm p}^2\right). \tag{45}$$

In this paper, we show some examples of the non-linear reconstructions (Figs 12 , 13, 14 and 15). As can be seen from these plots, the resolution of the reconstructions improves radically, down to the scale of large clusters. Comparing Figs 6 and 15 where the redshift

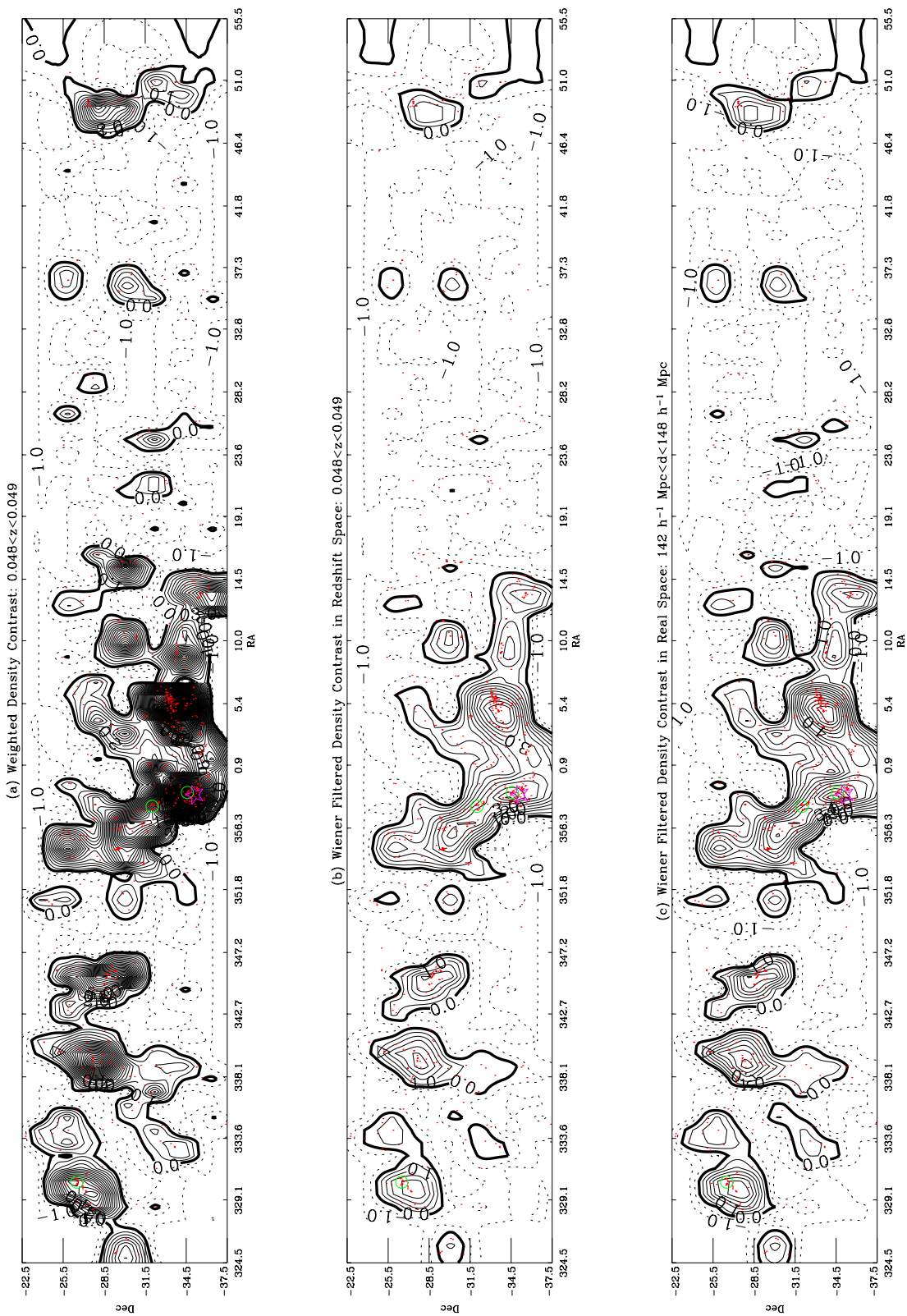

Figure 12. Reconstructions of the 2dFGRS SGP region for the redshift range $0.047 \leqslant z \leqslant 0.049$ for $5\,h^{-1}$ Mpc target cell size. The overdensity centred (1) on RA $\approx 336^{\circ}.5$, Dec. $\approx -30^{\circ}.0$ is SCSGP03 (see Table 1), (2) on RA $\approx 0^{\circ}.0$, Dec. $\approx -30^{\circ}.0$ is SCSGP04, and (3) on RA $\approx 36^{\circ}.0$, Dec. $\approx -29^{\circ}.3$ is SCSGP05. The underdensity centred (1) on RA $\approx 339^{\circ}.5$, Dec. $\approx -30^{\circ}.0$ is VSGP01, (2) on RA $\approx 351^{\circ}.5$, Dec. $\approx -29^{\circ}.3$ is VSGP02, (3) on RA $\approx 18^{\circ}.0$, Dec. $\approx -28^{\circ}.5$ is VSGP04, and (4) on RA $\approx 32^{\circ}.2$, Dec. $\approx -29^{\circ}.5$ is VSGP05 (see Table 2).

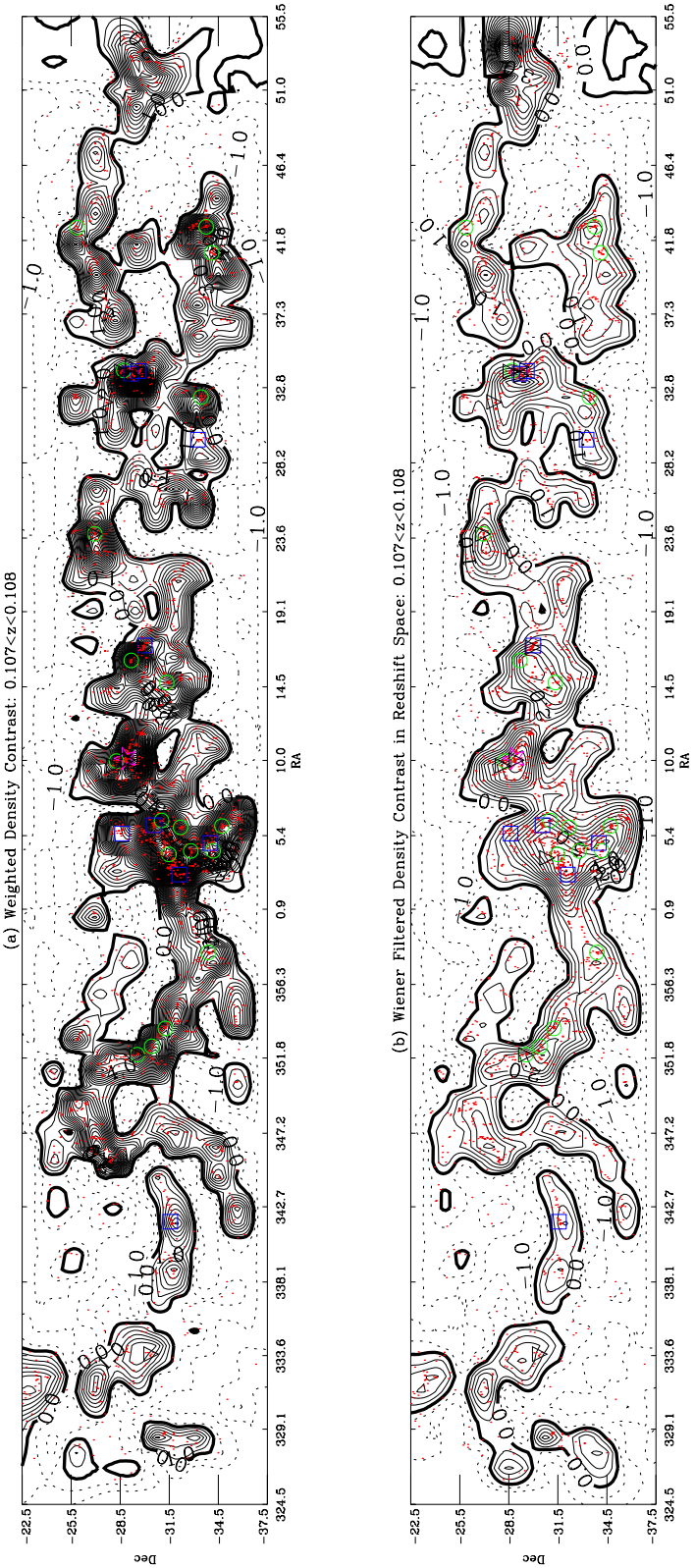

Figure 13. Reconstructions of the 2dFGRS SGP region for the redshift range $0.107 \leqslant z \leqslant 0.108$ for 5 h^{-1} Mpc target cell size. Same as in Fig. 3. The overdensity centred (1) on RA $\approx 1^{\rm h}7$, Dec. $\approx -31^{\circ}0$ is SCSGP16 (see Table 1), (2) on RA $\approx 36^{\rm h}3$, Dec. $\approx -30^{\circ}0$ is SCSGP15, and (3) on RA $\approx 345^{\circ}0$, Dec. $\approx -30^{\circ}0$ is SCSGP17. The underdensity centred (1) on RA $\approx 335^{\circ}0$, Dec. $\approx -35^{\circ}2$ is VSGP25 (see Table 2), (2) on RA $\approx 11^{\rm h}3$, Dec. $\approx -24^{\circ}5$ is VSGP22, and (3) on RA $\approx 48^{\rm h}0$, Dec. $\approx -30^{\circ}5$ is VSGP20.

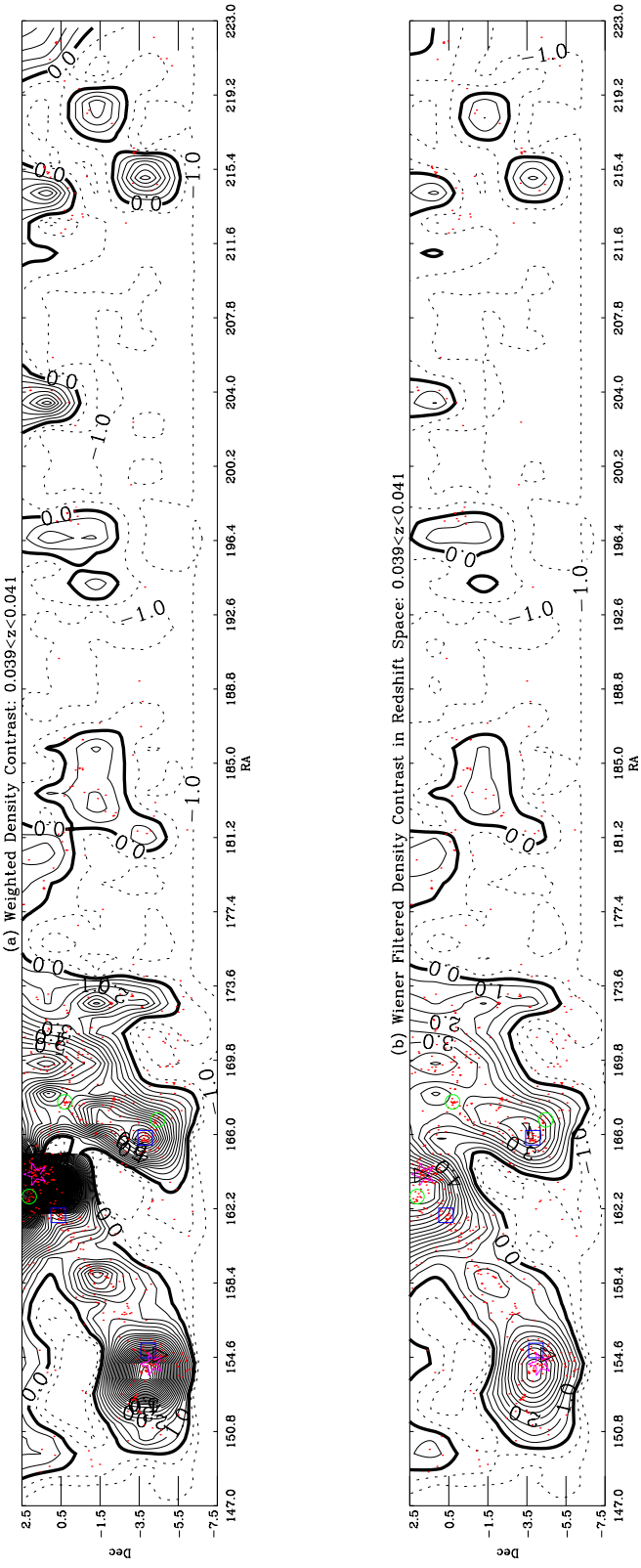

Figure 14. Reconstructions of the 2dFGRS NGP region for the redshift range $0.039 \leqslant z \leqslant 0.041$ for 5 h^{-1} Mpc target cell size. Same as in Fig. 3. The overdensity centred on RA $\approx 153^{\circ}.0$, Dec. $\approx -4^{\circ}.0$ is SCNGP01 and is part of the Shapley supercluster (see Table 1). The underdensities are VNGP01, VNGP02, VNGP03, VNGP04, VNGP05, VNGP06 and VNGP07 (see Table 3).

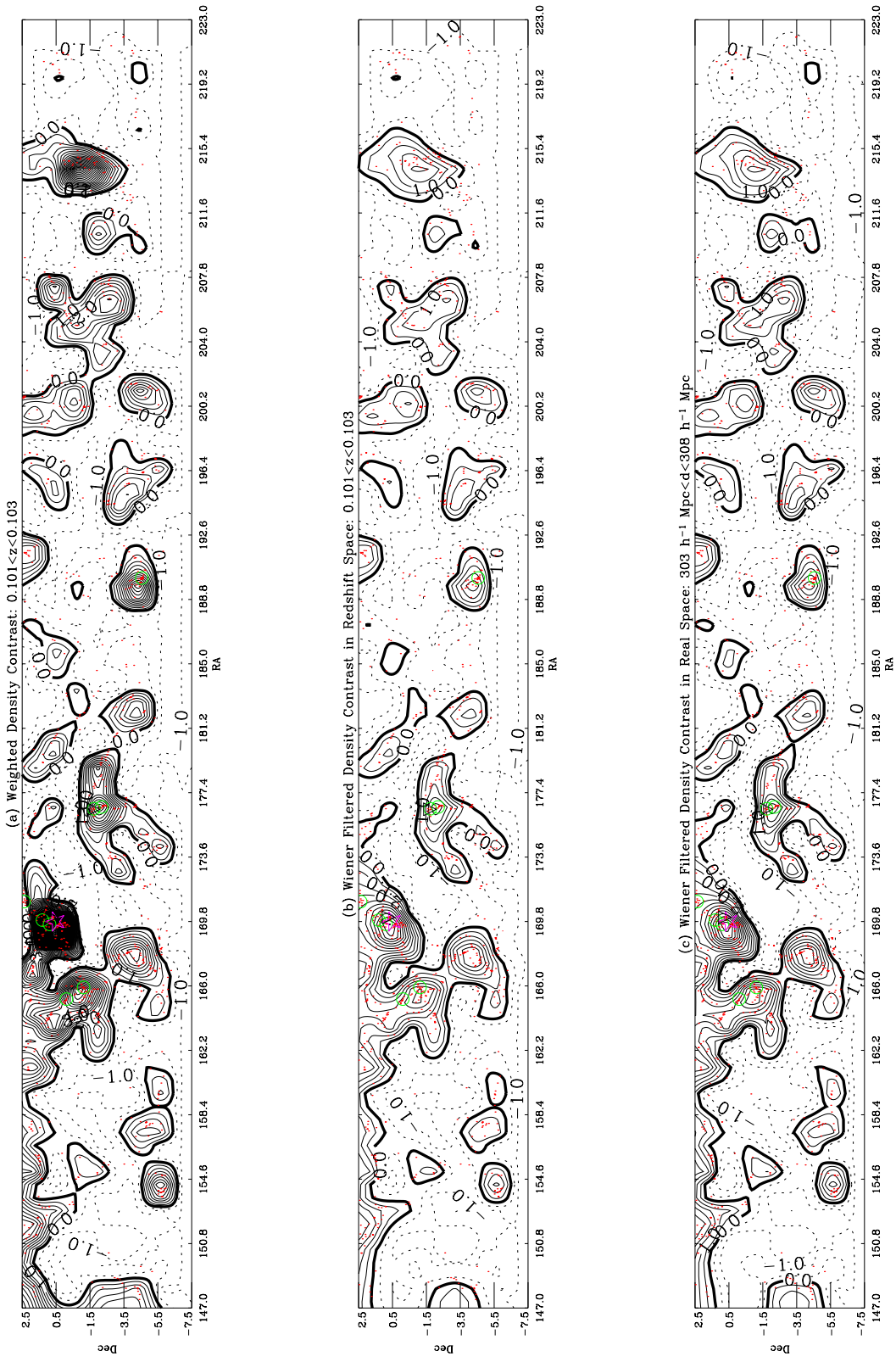

Figure 15. Reconstructions of the 2dFGRS NGP region for the redshift range $0.101 \leqslant z \leqslant 0.103$ for 5 h^{-1} Mpc target cell size. Same as in Fig. 3.

ranges of the maps are similar, we conclude that 10 and 5 h^{-1} Mpc resolutions give consistent reconstructions.

Due to the very large number of cells, we reconstruct four separate density fields for redshift ranges $0.035 \lesssim z \lesssim 0.05$ (4710 pixel) and $0.09 \lesssim z \lesssim 0.11$ (10 440 pixel) in the SGP, $0.035 \lesssim z \lesssim 0.05$ (2331 pixel) and $0.09 \lesssim z \lesssim 0.12$ (8379 pixel) in the NGP. There are 46 redshift slices in total. The χ^2 analysis of the density field yields $\chi^2/\mathrm{dof} = 0.54$ for these reconstructions. This low value reflects the systematic errors due to non-linear effects.

To investigate the effects of using different non-linear redshift distortion approximations, we also reconstruct one field without the damping function but just collapsing the Fingers of God. Although including the damping function results in a more physically accurate reconstruction of the density field in real space, it is still not enough to account for the elongation of the richest clusters along the line of sight. Collapsing the Fingers of God as well as including the damping function underestimates power, resulting in noisy reconstruction of the density field. We choose to use only the damping function for the non-linear scales obtaining stable results for the density field reconstruction.

The theory of gravitational instability states that as the dynamics evolve away from the linear regime, the initial field deviates from Gaussianity and skewness develops. The Wiener filter, in the form presented here, only minimizes the variance and it ignores the higher moments that describe the skewness of the underlying distribution. However, because the scales of reconstructions presented in this section are not highly non-linear and the signal-to-noise ratio is high, the assumptions involved in this analysis are not severely violated for the non-linear reconstruction of the density field in redshift space. The real-space reconstructions are more sensitive to the choice of cell size and the power spectrum because the Wiener filter is used not only for noise suppression but also for transformation from redshift space. Therefore, reconstructions in redshift space are more reliable on these non-linear scales than those in real space.

A different approach to the non-linear density field reconstruction presented in this paper is to apply the Wiener filter to the reconstruction of the logarithm of the density field, as there is good evidence that the statistical properties of the perturbation field in the quasi-linear regime are well approximated by a lognormal distribution. A detailed analysis of the application of the Wiener filtering technique to lognormal fields is given in Sheth (1995).

7 MAPPING THE LARGE-SCALE STRUCTURE OF THE 2DFGRS

One of the main goals of this paper is to use the reconstructed density field to identify the major superclusters and voids in the 2dFGRS. We define superclusters (voids) as regions of large overdensity (underdensity) which are above (below) a certain threshold. This approach has been used successfully by several authors (e.g. Saunders et al. 1991; Kolokotronis, Basilakos & Plionis 2002; Plionis & Basilakos 2002; Einasto et al. 2003a,b).

7.1 Superclusters

In order to find the superclusters listed in Table 1, we define the density contrast threshold, $\delta_{\rm th}$, as distance-dependent. We use a varying density threshold for two reasons that are related to the way the density field is reconstructed. First, the adaptive gridding we use implies that the cells become bigger with increasing redshift. This means that the density contrast in each cell decreases. The second effect that decreases the density contrast arises due to the Wiener filter signal tending to zero towards the edges of the survey. Therefore, for each redshift slice we find the mean and the standard deviation of the density field (averaged over 113 cells for the NGP and 223 for the SGP), then we calculate $\delta_{\rm th}$ as twice the standard deviation of the field added to its mean, averaged over the SGP and NGP for each redshift bin (see Fig. 16). In order to account for the clustering effects, we fit a smooth curve to $\delta_{\rm th}$, using χ^2 minimization. The best fit, also shown Fig. 16, is a quadratic equation with $\chi^2/(\text{number of dof}) = 1.6$. We use this fit when selecting the overdensities. We note that choosing a smoothed or unsmoothed density threshold does not change the selection of the superclusters.

The list of superclusters in the SGP and NGP regions are given in Table 1. This table is structured as follows. Column 1 is the identification, columns 2 and 3 are the minimum and the maximum redshift, columns 4 and 5 are the minimum and maximum RA, columns 6 and 7 are the minimum and maximum Dec. over which the density contours above $\delta_{\rm th}$ extend. In column 8, we show the number of Durham groups with more than nine members that the supercluster contains. In column 9, we show the number of Abell, APM and EDCC clusters studied by De Propris et al. (2002) which the supercluster has. In the last column, we show the total number of groups and clusters. Note that most of the Abell clusters are counted in the Durham group catalogue. We observe that the rich groups (groups with more than nine members) almost always reside in superclusters whereas poorer groups are more dispersed. We note that the superclusters that contain Abell clusters are on average richer than superclusters that do not contain Abell clusters, in agreement with Einasto et al. (2003b). However, we also note that the number of Abell clusters in a rich supercluster can be equal to the number of Abell clusters in a poorer supercluster, whereas the number of Durham groups increases as the overdensity increases. Thus, we conclude that the Durham groups are in general better representatives of the underlying density distribution of the 2dFGRS than Abell clusters.

The superclusters SCSGP03, SCSGP04 and SCSGP05 can be seen in Fig. 3. SCSGP04 is part the rich Pisces–Cetus supercluster which was first described by Tully (1987). SCSGP01, SCSGP02, SCSGP03 and SCSGP04 are all filamentary structures connected to each other, forming a multibranching system. SCSGP05 seems to be a more isolated system, possibly connected to SCSGP06 and SCSGP07. SCSGP06 (Fig. 4) is the upper part of the gigantic Horoglium Reticulum supercluster. SCSGP07 (Fig. 4) is the extended part of the Leo–Coma supercluster. The richest supercluster in the SGP region is SCSGP16, which can be seen in the middle of the plots in Fig. 13. Also shown, in the same figure, is SCSGP15, one of the richest superclusters in the SGP and the edge of SCSGP17. In fact, as evident from Fig. 13, SCSGP14, SCSGP15, SCSGP16 and SCSGP17 are branches of one big filamentary structure. In Fig. 14, we see SCNGP01; this structure is part of the upper edge of the Shapley supercluster. The richest supercluster in the NGP is SCNGP06, shown in Fig. 5. This supercluster was also identified by Einasto et al. (2001) in the Las Campanas Redshift Survey (SCL 126 in the list) and in the SDSS (Einasto et al. 2003b; N13 in Table 3). Around SCNGP06, in the neighbouring redshift slices, there are two rich filamentary superclusters, SCNGP06 and SCNGP08 (Fig. 6). SCNGP07 seems to be the node point of these filamentary structures. The superclusters found in the south are, in general, richer than the those found in the north. This is probably

Table 1. The list of superclusters.

No	$z_{\min}$	$z_{\max}$	$\mathrm{RA}_{\min}$ (1950) (°)	$\mathrm{RA}_{\max}$ (1950) (°)	$\mathrm{Dec}_{\min}$ (1950) (°)	$\mathrm{Dec}_{\max}$ (1950) (°)	$N_{\mathrm{gr}} \geqslant 9$	N_{clus}	N_{total}
SCSGP01	0.048	0.054	348.5	356.8	−37.5	−25.5	23	9	27
SCSGP02	0.054	0.057	337.3	0.0	−35.5	−33.0	9	1	9
SCSGP03	0.057	0.064	330.6	342.5	−37.5	−22.5	23	8	26
SCSGP04	0.057	0.068	350.0	10.0	−35.5	−24.0	34	14	37
SCSGP05	0.054	0.064	32.5	39.0	−33.0	−25.5	14	7	18
SCSGP06	0.064	0.082	45.5	55.0	−35.0	−24.0	26	7	31
SCSGP07	0.064	0.071	18.5	40.0	−35.0	−31.0	10	4	11
SCSGP08	0.068	0.075	321.5	327.0	−35.0	−22.5	9	3	11
SCSGP09	0.075	0.082	333.0	342.5	−37.5	−22.5	20	9	24
SCSGP10	0.082	0.093	342.5	350.5	−36.0	−29.0	18	9	21
SCSGP11	0.086	0.097	327.0	333.0	−34.5	−24.0	14	4	15
SCSGP12	0.093	0.097	338.0	342.6	−36.0	−34.8	4	1	5
SCSGP13	0.093	0.097	0.0	3.8	−36.0	−34.8	3	0	3
SCSGP14	0.093	0.104	16.0	24.6	−33.0	−28.2	8	1	8
SCSGP15	0.097	0.115	28.0	44.6	−35.2	−24.6	34	18	41
SCSGP16	0.100	0.119	1.5	21.9	−35.2	−26.5	93	20	98
SCSGP17	0.100	0.108	332.9	357.0	−35.2	−26.5	38	7	43
SCSGP18	0.150	0.166	1.5	31.8	−33.0	−26.5	18	6	22
SCSGP19	0.162	0.177	22.8	34.5	−35.2	−24.6	13	5	15
SCSGP20	0.181	0.202	342.5	356.5	−35.5	−24.6	13	4	14
SCNGP01	0.035	0.068	147.5	174.5	−6.5	2.5	59	6	61
SCNGP02	0.048	0.061	210.0	218.5	−5.0	0.0	19	0	19
SCNGP03	0.068	0.075	150.0	155.0	−1.0	2.5	6	0	6
SCNGP04	0.068	0.075	158.0	166.5	−1.0	2.5	8	1	9
SCNGP05	0.071	0.082	171.0	184.0	−3.5	2. 5	27	6	28
SCNGP06	0.079	0.094	185.0	202.5	−7.5	2.5	77	7	79
SCNGP07	0.086	0.101	147.0	181.5	−5.5	2.5	31	4	34
SCNGP08	0.090	0.131	165.0	185.0	−6.3	2.5	51	10	57
SCNGP09	0.103	0.114	158.5	163.0	−1.3	2.5	8	1	9
SCNGP10	0.103	0.118	197.0	203.0	−3.75	1.25	22	0	22
SCNGP11	0.123	0.131	147.0	173.0	0.0	2.5	3	2	3
SCNGP12	0.119	0.142	210.0	219.0	−4.0	1.3	19	2	20
SCNGP13	0.131	0.142	173.0	179.0	−6.25	−1.3	5	2	6
SCNGP14	0.131	0.142	185.0	193.0	−6.25	1.3	7	0	7
SCNGP15	0.131	0.138	155.0	160.0	−6.3	1.3	9	1	9
SCNGP16	0.142	0.146	166.0	174.0	−0.3	1.3	5	0	5
SCNGP17	0.142	0.146	194.0	199.0	−2.5	1.3	1	0	1
SCNGP18	0.146	0.150	204.0	210.0	−2.5	1.3	4	0	4
SCNGP19	0.173	0.177	181.0	184.0	−1.0	−4.0	3	0	3
SCNGP20	0.181	0.185	185.5	193.0	−1.0	−4.0	1	0	1

because the SGP region has a lower flux limit than the NGP and therefore probes deeper.

Table 1 shows only the major overdensities in the survey. These tend to be filamentary structures that are mostly connected to each other.

7.2 Voids

For the catalogue of the largest voids in Tables 2 and 3, we only consider regions with 80 per cent completeness or more and go up to a redshift of 0.15. Following the previous studies (e.g. El-Ad & Piran 2000; Benson et al. 2003; Sheth et al. 2003), our chosen underdensity threshold is $\delta_{\mathrm{th}} = -0.85$. The tables of voids are structured in a similar way as the table of superclusters, only we give separate tables for the NGP and SGP voids. The most intriguing structures seen are the voids VSGP01, VSGP2, VSGP03, VSGP4 and VSGP05. These voids, clearly visible in the radial number density function of the 2dFGRS, are actually part of a big superhole broken up by the low value of the void density threshold. This superhole has been observed and investigated by several authors (e.g. Cross et al. 2001; De Propris et al. 2002; Norberg et al. 2002; Frith et al. 2003). The local NGP region also has excess underdensity (VNGP01,VNGP02, VNGP03, VNGP04, VNGP05, VNGP06 and VNGP07, again part of a big superhole) but the voids in this area are not as big or as empty as the voids in the local SGP. In fact, by combining the results from the Two-Micron All-Sky Survey, the Las Campanas Survey and the 2dFGRS, Frith et al. (2003) conclude that these underdensities suggest that there is a contiguous void stretching from north to south. If such a void does exist, then it is unexpectedly large for our present understanding of large-scale structure, where on large enough scales the Universe is isotropic and homogeneous.

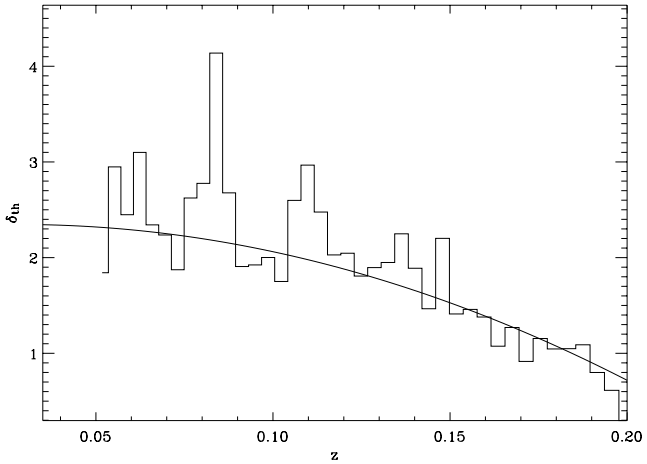

Figure 16. The density threshold δ_{th} as a function of redshift z and the best-fitting model used to select the superclusters in Table 1.

Table 2. The list of voids in the SGP.

No	z_{min}	z_{max}	RA_{min} (1950) (°)	RA_{max} (1950) (°)	Dec_{min} (1950) (°)	Dec_{max} (1950) (°)
VSGP01	0.035	0.051	332.5	342.7	−37.5	−22.5
VSGP02	0.035	0.051	342.7	0.0	−33.0	−25.5
VSGP03	0.035	0.048	0.9	11.5	−34.5	−28.5
VSGP04	0.035	0.051	12.4	23.6	−30.5	−26.0
VSGP05	0.035	0.054	23.6	40.8	−33.5	−26.0
VSGP06	0.035	0.042	32.8	37.3	−33.5	−28.5
VSGP07	0.035	0.051	39.5	46.4	−31.5	−28.5
VSGP08	0.035	0.042	46.4	51.0	−31.5	−28.5
VSGP09	0.039	0.044	324.5	330.0	−34.5	−28.5
VSGP10	0.039	0.041	10.0	17.5	−33.5	−29.5
VSGP11	0.041	0.044	15.5	22.5	−33.5	−28.5
VSGP12	0.057	0.061	347.2	351.8	−31.5	−28.5
VSGP13	0.082	0.086	5.4	8.0	−31.5	−28.5
VSGP15	0.082	0.089	41.8	49.3	−31.5	−28.5
VSGP16	0.086	0.089	12.5	16.3	−31.5	−28.5
VSGP17	0.086	0.089	31.0	33.5	−32.5	−28.5
VSGP18	0.089	0.097	351.8	354.05	−30.5	−29.5
VSGP19	0.089	0.093	42.7	45.5	−30.5	−29.5
VSGP20	0.093	0.104	46.4	52.5	−32.5	−28.2
VSGP21	0.093	0.100	28.2	32.8	−31.5	−28.5
VSGP22	0.097	0.104	7.7	12.5	−32.0	−28.5
VSGP23	0.097	0.100	347.2	348.5	−32.0	−28.5
VSGP24	0.100	0.108	328.2	334.7	−28.5	−25.5
VSGP25	0.100	0.112	334.7	338.1	−34.5	−33.0
VSGP26	0.112	0.119	353.0	356.3	−31.5	−28.5
VSGP27	0.112	0.115	1.5	5.4	−30.0	−27.0
VSGP28	0.112	0.115	25.9	28.2	−30.0	−27.0
VSGP29	0.112	0.115	41.0	46.4	−30.0	−27.0
VSGP30	0.115	0.119	26.2	30.5	−34.5	−31.5
VSGP31	0.119	0.123	325.0	329.2	−28.5	−25.5
VSGP32	0.119	0.123	333.0	334.5	−28.5	−26.5
VSGP33	0.119	0.123	347.2	350.0	−28.5	−25.5
VSGP34	0.119	0.123	41.5	49.3	−38.8	−31.8
VSGP35	0.119	0.127	11.2	16.5	−28.2	−27.5
VSGP36	0.123	0.131	333.6	337.6	−31.5	−28.5
VSGP37	0.123	0.127	347.2	351.8	−30.0	−27.0
VSGP38	0.131	0.142	333.6	340.5	−34.5	−31.5
VSGP39	0.131	0.138	32.3	37.5	−35.2	−24.8
VSGP40	0.138	0.142	30.3	33.5	−33.5	−29.0

Table 3. The list of voids in the NGP.

No	z_{min}	z_{max}	RA_{min} (1950) (°)	RA_{max} (1950) (°)	Dec_{min} (1950) (°)	Dec_{max} (1950) (°)
VNGP01	0.035	0.054	147.0	160.0	−4.0	1.5
VNGP02	0.035	0.041	166.0	171.0	−1.0	2.5
VNGP03	0.035	0.046	171.0	181.2	−1.5	2.5
VNGP04	0.035	0.051	183.0	189.0	−1.5	2.5
VNGP05	0.035	0.046	189.0	197.0	−1.5	2.0
VNGP06	0.035	0.046	202.2	206.0	−1.5	2.0
VNGP07	0.037	0.046	204.2	215.6	−2.0	0.0
VNGP08	0.041	0.051	163.8	169.8	−4.5	2.5
VNGP09	0.049	0.061	177.0	196.4	−3.5	2.5
VNGP10	0.054	0.057	165.5	173.0	−1.5	2.5
VNGP11	0.057	0.061	163.5	166.0	0.0	1.5
VNGP12	0.054	0.061	206.0	208.0	−1.5	0.5
VNGP13	0.071	0.075	176.0	179.0	−1.0	0.5
VNGP14	0.079	0.094	186.5	204.2	−7.5	0.5
VNGP15	0.092	0.097	150.8	160.2	−7.5	−6.0
VNGP16	0.093	0.100	147.0	149.5	−6	1.5
VNGP17	0.094	0.101	204.0	211.5	−3.5	2.5
VNGP18	0.099	0.115	147.5	153.6	−4.0	1.0
VNGP19	0.099	0.120	188.8	197.0	−3.0	2.5
VNGP20	0.112	0.120	176.6	178.0	0.5	2.5
VNGP21	0.110	0.115	211.6	217.0	−2.5	−0.5
VNGP22	0.110	0.123	200.2	205.0	−3.25	2.5
VNGP23	0.123	0.131	169.0	174.0	−4.0	−1.25
VNGP24	0.127	0.131	182.5	188.0	0.0	2.5
VNGP25	0.127	0.131	197.5	202.0	−1.25	0.5
VNGP26	0.134	0.142	179.5	187.5	−2.0	2.5
VNGP27	0.134	0.138	204.0	207.0	−1.5	0.0
VNGP28	0.138	0.150	147.0	154.6	−3.5	2.5
VNGP29	0.142	0.150	162.0	166.0	−4.0	1.5
VNGP30	0.142	0.150	172.6	178.0	−1.0	2.5

8 DISCUSSION AND SUMMARY

In this paper we use the Wiener filtering technique to reconstruct the density field of the 2dFGRS. We pixelize the survey into igloo cells bounded by RA, Dec. and redshift. The cell size varies in order to keep the number of galaxies per cell roughly constant and is approximately 10 and 5 h^{-1} Mpc for the high- and low-resolution maps, respectively, at the median redshift of the survey. Assuming a prior based on parameters $\Omega_m = 0.3$, $\Omega_\Lambda = 0.7$, $\beta = 0.49$, $\sigma_8 = 0.8$ and $\Gamma = 0.2$, we find that the reconstructed density field clearly picks out the groups catalogue built by Eke et al. (2003) and the Abell, APM and EDCC clusters investigated by De Propris et al. (2002). We also reconstruct four separate density fields with different redshift ranges for a smaller cell size of 5 h^{-1} Mpc at the median redshift. For these reconstructions, we assume a non-linear power spectrum fit developed by Smith et al. (2003) and linear biasing. The resolution of the density field improves dramatically, down to the size of big clusters. The derived high-resolution density fields are in agreement with the lower-resolution versions.

We use the reconstructed fields to identify the major superclusters and voids in the SGP and NGP. We find that the richest superclusters are filamentary and multibranching, in agreement with Einasto et al. (2003a). We also find that the rich clusters always reside in superclusters whereas poor clusters are more dispersed. We present the major superclusters in the 2dFGRS in Table 1. We pick out two very rich superclusters, one in the SGP and one in the NGP. We also identify voids as underdensities that are below $\delta \approx -0.85$ and

that lie in regions with more that 80 per cent completeness. These underdensities are presented in Table 2 (SGP) and Table 3 (NGP). We pick out two big voids, one in the SGP and one in the NGP. Unfortunately, we cannot measure the sizes and masses of the large structures we observe in the 2dF as most of these structures continue beyond the boundaries of the survey.

The detailed maps and lists of all of the reconstructed density fields and plots of the residual fields can be found on the WWW at http://www.ast.cam.ac.uk/∼pirin.

One of the main aims of this paper is to identify the large-scale structure in the 2dFGRS. The Wiener filtering technique provides a rigorous methodology for variable smoothing and noise suppression. As such, a natural continuation of this work is using the Wiener filtering method in conjunction with other methods to further investigate the geometry and the topology of the supercluster–void network. Sheth et al. (2003) have developed a powerful surface modelling scheme, SURFGEN, in order to calculate the Minkowski functionals of the surface generated from the density field. The four Minkowski functionals – the area, the volume, the extrinsic curvature and the genus – contain information about the geometry, connectivity and topology of the surface (cf. Mecke, Buchert & Wagner, 1994; Sheth et al. 2003) and thus they will provide a detailed morphological analysis of the superclusters and voids in the 2dFGRS.

As mentioned before, the Wiener filter has its limitations. The main shortcoming of the method is that it predicts the mean field in the absence of data, biasing the reconstruction towards zero. This is due to the conservative nature of the technique; it replaces noise by zero field. To avoid this bias, Zaroubi (2002) have proposed a new linear unbiased minimal variance (UMV) estimator. The UMV estimator is constructed in a similar way to the Wiener filter but with an additional constraint of an unbiased mean underlying field. This estimator, unlike the Wiener filter, does not alter the reconstructed field at the data points but lacks the noise suppression aspect. The bias of the Wiener filter is somewhat remedied by the pixelization scheme used, where the cell sizes vary to keep noise level in each cell roughly equal. This way, the reconstructed density field is less biased towards the null field, because there are no pixels which do not contain any data points. The varying pixelization procedure also allows the reconstruction of a much bigger volume than if we had used fixed size pixels. However, varying the size of cells does complicate the cosmography (e.g. having to vary the supercluster density threshold with distance). We are currently reconstructing a part of the density field with fixed-sized cubes in Cartesian space. We will present our results in a forthcoming paper (Sheth et al., in preparation).

Although not applicable to the 2dFGRS, the Wiener reconstruction technique is well suited to recovering the velocity fields from peculiar velocity catalogues. Comparisons of galaxy density and velocity fields allow direct estimations of the cosmological parameters such as the bias parameter and the mean mass density. These comparisons will be possible with the upcoming 6dF Galaxy Survey (http://www.mso.anu.edu.au/6dFGS) which will measure the redshifts of 170 000 galaxies and the peculiar velocities of 15 000 galaxies by 2005 June. Compared to the 2dFGRS, the 6dF survey has a much higher sky coverage (the entire southern sky down to $|b| > 10^\circ$). This wide survey area will allow a full hemispheric Wiener reconstruction of large-scale structure so that the sizes and masses of the superclusters and voids can be determined.

ACKNOWLEDGMENTS

We thank Yehuda Hoffman for his useful comments. The 2dFGRS was made possible through the dedicated efforts of the staff at Anglo-Australian Observatory, both in crediting the 2dF instrument and supporting it on the telescope. PE acknowledges support from the Middle East Technical University, Ankara, Turkey, the Turkish Higher Education Council and Overseas Research Trust. OL and JAP acknowledge the Particle Physics and Astronomy Research Council (PPARC) for their Senior Research Fellowships. This research was conducted utilizing the supercomputer COSMOS at the Department of Applied Mathematics and Theoretical Physics (DAMTP), Cambridge.

REFERENCES

Ballinger W. E., Peacock J. A., Heavens A. F., 1996, MNRAS, 282, 877
Benson A., Hoyle F., Torres F., Vogeley M., 2003, MNRAS, 340, 160
Bond J. R., Kofman L., Pogosyan D., 1996, Nat, 380, 603
Bouchet F. R., Gispert R., 1999, New Astron., 4, 443
Bunn E., Fisher K. B., Hoffman Y., Lahav O, Silk J., Zaroubi S., 1994, ApJ, 432, L75
Colless M. et al., 2001, MNRAS, 328, 1039
Cross M. et al., 2001, MNRAS, 324, 825
Davis M., Huchra J. P., 1982, ApJ, 254, 437
De Propris R. et al., 2002, MNRAS, 329, 87
Efstathiou G., Moody S., 2001, MNRAS, 325, 1603
Einasto M., Einasto J., Tago E., Müller V., Andernach H., 2001, AJ, 122, 2222
Einasto J., Hütsi G., Einasto G., Saar E., Tucker D. L., Müller V., Heinämäki P., Allam S. S., 2003a, A&A, 405, 425
Einasto J. et al., 2003b, A&A, 410, 425
Eisenstein D. J., Hu W., 1998, ApJ, 518, 2
Eke V. et al., 2003, MNRAS, submitted
El-Ad H., Piran T., 2000, MNRAS, 313, 553
Fisher K. B., Lahav O., Hoffman Y., Lynden-Bell D., Zaroubi S., 1995, MNRAS, 272, 885
Freedman W. L. et al., 2001, ApJ, 553, 47
Frith W. J., Busswell G. S., Fong R., Metcalfe N., Shanks T., 2003, MNRAS, 345, 1049
Hawkins E. et al., 2003, MNRAS, 346, 78
Kaiser N., 1987, MNRAS, 227, 1
Kang X., Jing Y. P., Mo H. J., Börner G., 2002, MNRAS, 336, 892
Kolokotronis V., Basilakos S., Plionis M., 2002, MNRAS, 331, 1020
Lahav O. et al., 2002, MNRAS, 333, 961
Lahav O., Fisher K. B., Hoffman Y., Scharf C. A., Zaroubi S., 1994, ApJ, 423, L93
Maddox S. J., Efstathiou G., Sutherland W. J., 1990, MNRAS, 246, 433
Madgwick D. et al., 2002, MNRAS, 333, 133
Mecke K. R., Buchert T., Wagner H., 1994, A&A, 288, 697
Moody S., 2003, PhD thesis, Univ. Cambridge
Nusser A., Davis M., 1994, ApJ, 421, L1
Norberg P. et al., 2002, MNRAS, 332, 827
Peacock J. A., Dodds S. J., 1994, MNRAS, 267, 1020
Peacock J. A., Dodds S. J., 1996, MNRAS, 280, L19
Peacock J. A., Smith R. E., 2000, MNRAS, 318, 1144
Percival W. et al., 2001, MNRAS, 327, 1297
Plionis M., Basilakos S., 2002, MNRAS, 330, 339
Press W. H., Vetterling W. T., Teukolsky S. A., Flannery B. P., 1992, Numerical Recipes in FORTRAN 77, 2nd edn. Cambridge Univ. Press, Cambridge
Rybicki G. B., Press W. H., 1992, ApJ, 398, 169
Saunders W., Frenk C., Rowan-Robinson M., Lawrence A., Efstathiou G., 1991, Nat, 349, 32

Schmoldt I. M. et al., 1999, AJ, 118, 1146
Seljak U., 2000, MNRAS, 318, 119
Sheth R. K., 1995, MNRAS, 264, 439
Sheth J. V., Sahni V., Shandarin S. F., Sathyaprakah B. S., 2003, MNRAS, 343, 22
Smith R. E. et al., 2003, MNRAS, 341, 1311
Tegmark M., Efstathiou G., 1996, MNRAS, 281, 1297
Tully B., 1987, Atlas of Nearby Galaxies. Cambridge Univ. Press, Cambridge
Verde L. et al., 2002, MNRAS, 335, 432
Wiener N., 1949, Extrapolation and Smoothing of Stationary Time Series. Wiley, New York
Yahil A., Strauss M. A., Huchra J. P., 1991, ApJ, 372, 380
Zaroubi S., 2002, MNRAS, 331, 901
Zaroubi S., Hoffman Y., 1996, ApJ, 462, 25
Zaroubi S., Hoffman Y., Fisher K., Lahav O., 1995, ApJ, 449, 446
Zehavi I. et al., 2002, ApJ, 501, 172

This paper has been typeset from a TEX/LATEX file prepared by the author.